

Physics-Informed Spatial-Temporal Transformer for Terahertz Near-Field Beam Tracking

Zhi Zeng, *Student Member, IEEE*, Chong Han, *Senior Member, IEEE*, and Emil Björnson, *Fellow, IEEE*

Abstract—Terahertz (THz) ultra-massive multiple-input multiple-output (UM-MIMO) promises ultra-high throughput, while its highly directional beams demand rapid and accurate beam tracking driven by precise user-state estimation. Moreover, large array apertures at high frequencies induce near-field propagation effects, where far-field modeling becomes inaccurate and near-field parametric channel estimation is costly. Bypassing near-field codebook, PAST-TT is proposed to bridge near-field tracking with low-overhead far-field codebook probing by exploiting parallax, amplified by widely spaced subarrays. With comb-type frequency-division multiplexing pilots, each subarray yields frequency-affine phase signatures whose frequency and temporal increments encode propagation delay and its variation between frames. Building on these signatures, a Parallax-Aware Spatial Transformer (PAST) compresses them and outputs per-frame position estimates with token reliability to downweight bad frames, regularized by a physics-in-the-loop consistency loss. A causal Temporal Transformer (TT) then performs reliability-aware filtering and prediction over a sliding window to initialize the beam of the next frame. Acting on short token sequences, PAST-TT avoids a monolithic spatial-temporal network over raw pilots, which keeps the model lightweight with a critical path latency of 0.61 ms. Simulations show that at 15 dB signal-to-noise ratio, PAST achieves 7.81 mm distance RMSE and 0.0588° angle RMSE. Even with a bad-frame rate of 0.1, TT reduces the distance and angle prediction RMSE by 23.1% and 32.8% compared with the best competing tracker.

Index Terms—Terahertz communications, near-field, beam tracking, physics-informed deep learning.

I. INTRODUCTION

TERAHERTZ (THz) communications have emerged as an attractive component for future wireless systems, as the ultra-broad spectrum from 0.1 THz to 10 THz provides abundant bandwidth and opens the door to extreme-capacity wireless links [2]. Nevertheless, the notable path loss in the THz band can affect the link budget and limit coverage [3]. Fortunately, the short wavelength enables dense integration and ultra-large apertures, making ultra-massive multiple-input multiple-output (UM-MIMO) a natural companion to THz for harvesting substantial beamforming gains and compensating for the severe propagation loss [4]. To make THz UM-MIMO

practical, hybrid beamforming (HBF) with a limited number of RF chains is typically adopted for hardware efficiency, which constrains how many beams can be probed simultaneously and makes low-overhead training imperative [5], [6]. However, the resulting pencil beams are highly sensitive to mobility and channel dynamics, and even modest pointing errors can cause severe throughput degradation [7]–[9]. Consequently, accurate beam alignment and tracking become essential, requiring frequent beam updates based on the time-varying user state under tight per-frame latency and training overhead constraints.

Furthermore, this alignment requirement becomes more challenging because large array apertures at high carrier frequencies confine THz links into the radiative near-field (NF), where the conventional far-field (FF) plane-wave model (PWM) is inaccurate due to non-negligible wavefront curvature, whereas element-wise spherical-wave model (SWM) can be computationally prohibitive for UM-MIMO [8]–[12]. Additionally, in THz links with a dominant line-of-sight (LoS) path, NF beams depend jointly on angle and distance, which substantially enlarges the search space for beam management and makes joint angle-distance sweeping prohibitively expensive for low-latency tracking [10], [13]. Meanwhile, practical training observations can be unreliable due to intermittent blockage and other impairments, further destabilizing online tracking if not properly detected and handled.

Taken together, these considerations underscore an urgent need for NF beam tracking mechanisms that simultaneously achieve high accuracy, strong robustness to occasional unreliable frames, and low control latency under practical THz UM-MIMO architectures.

A. Related Work

Extremely large apertures at THz bands move a non-negligible portion of propagation from purely FF into the radiative NF, where wavefront curvature breaks the FF plane-wave abstraction and makes beamforming and channel acquisition jointly depend on angle and distance [8]–[12]. Accordingly, extensive efforts revisit beam training and alignment under NF channel models and polar-domain representations that parameterize paths by direction and distance [8]–[12], [14], [15]. To reduce the prohibitive two-dimensional search burden, hierarchical training and structured NF codebooks have emerged, including spatial-chirp [16] and multi-stage refinement strategies that progressively narrow down the candidate region in the angle-distance domain [11], [14]. Related works also consider staged refinement that first leverages FF-like probing to confine angular candidates and then applies

An earlier version of this paper will be presented in part at the IEEE ICASSP, May 2026 [1].

Zhi Zeng is with the Terahertz Wireless Communications (TWC) Laboratory, Shanghai Jiao Tong University, Shanghai 200240, China (e-mail: zhi.zeng@sjtu.edu.cn).

Chong Han is with the Terahertz Wireless Communications (TWC) Laboratory and also the Cooperative Medianet Innovation Center (CMIC), School of Information Science and Electronic Engineering, Shanghai Jiao Tong University, Shanghai 200240, China (e-mail: chong.han@sjtu.edu.cn).

Emil Björnson is with the Department of Communication Systems, KTH Royal Institute of Technology, 100 44 Stockholm, Sweden (e-mail: emilbj@kth.se).

NF-aware processing to refine distance parameters, aiming to balance modeling accuracy and training complexity [17].

In addition, polar-domain codebook size and search overhead can scale sharply with the number of antennas, mobility and HBF constraints, which becomes particularly challenging for per-frame beam updates under tight control-latency budgets [15]. Beyond one-shot alignment, NF beam tracking has also started to attract attention, for example, by combining kinematic modeling with recursive estimators under hybrid architectures [12]. Nevertheless, many NF beam-management approaches still rely on searching over a large polar-domain candidate set to resolve distance-dependent focusing [11], [15]. This leaves a gap for fast beam management: *extracting NF geometric evidence under a lightweight probing budget without committing to NF codebook sweeping*.

In practical THz UM-MIMO deployments, unified probing over a wide distance range is favored, motivating NF tracking designs to operate with FF discrete Fourier transform (DFT) codebook probing [18]. Specifically, several works revisit the long-standing assumption that FF codebooks are unsuitable in the NF, and show that FF DFT probing can still expose distance-sensitive signatures through beam-response patterns, enabling NF alignment with reduced overhead [8], [9], [19]. In parallel, widely-spaced multi-subarray (WSMS) architectures have been advocated as practical THz front-ends that preserve high per-subarray gain while exploiting inter-subarray phase diversity, thereby enriching NF geometric information compared to co-located arrays [6]. Performance analyses further quantify such benefits by relating angle-distance accuracy to the multi-view aperture created by the subarray layout [20]. Closely related, position- or geometry-aided beam management leverages user-state information to reduce beam selection overhead in highly directional systems [21].

Despite these advances, existing solutions are often developed for one-shot alignment or isolated estimation tasks, and it remains underexplored how to convert low-overhead probing outcomes into a persistent and trackable measurement representation that can be robustly consumed by an online tracker under intermittent impairments. This motivates a second gap: *a structured handoff from FF probing to NF tracking that carries forward geometry evidence together with a principled notion of measurement reliability*.

After initial access, beam tracking aims to maintain alignment for mobile users with minimal overhead by exploiting temporal correlation in positions, path gains, or other low-dimensional channel parameters [22]. Kalman-type trackers perform recursive prediction and correction using sounding-beam observations, and robust extensions add realignment triggers and outlier rejection to mitigate loss of track under blockage and intermittent observations [23]–[26]. In parallel, deep learning (DL) has been increasingly explored for beam tracking, where sequence models map historical pilots or channel state information to future beams [27]. Beyond end-to-end predictors, learning-augmented filtering preserves the recursive Bayesian prediction-update structure, while using neural networks to learn key components that are difficult to model accurately, such as the Kalman gain [28]. More recently, DL has also been applied to NF and UM-MIMO beam

training and tracking, typically by CNN-assisted hierarchical training and RNN-based tracking coupled with sweeping [29], [30]. Nevertheless, many learning-based designs still treat measurements as high-dimensional black box inputs or rely on additional probing to explore the joint angle-distance space.

While these methods can improve accuracy in challenging dynamics, online deployment in highly directional THz systems still relies on strict causality, robustness against sporadic bad frames and tight inference latency within millisecond-scale control loops. Moreover, much of the tracking literature is rooted in FF angle-only abstractions [24], [25], whereas NF tracking involves angle-distance coupling and regime-dependent measurement structures. Therefore, it remains underexplored to address the third gap: *an end-to-end NF tracking loop that is explicitly reliability-aware and latency-conscious under practical THz beam management budgets*.

B. Contributions

In this work, we enable THz NF beam tracking through parallax under lightweight FF DFT probing. To form a tracking-ready interface from comb-type frequency-division multiplexing (FDM) pilots, we design a parallax-aware spatial transformer (PAST) for one-shot NF localization and reliability-aware tokenization. Then, we develop a causal temporal transformer (TT) to close the online beam tracking loop, leading to PAST-TT. The main contributions are summarized as follows.

- **We establish a parallax bridge that enables NF tracking under a lightweight FF probing budget.** Under a widely-spaced-subarray architecture with comb-type FDM pilots, we consider a hybrid spherical- and planar-wave channel model (HSPM). The phase signature of each subarray exhibits an approximately frequency-affine structure, and its adjacent-tone and inter-frame increments encode the propagation delay and its variation between frames. This leads to structured space-frequency-time evidence that supports low-overhead geometric inference without exhaustive joint angle-distance sweeping.
- **We propose the PAST as a physics-informed measurement encoder with explicit reliability-aware tokenization.** Leveraging the above evidence structure, high-dimensional pilots are distilled into compact physical tokens that preserve parallax and provide reliability statistics, suppressing intermittently corrupted observations without relying on fragile phase unwrapping. Geometry-biased, reliability-gated attention and a physics-in-the-loop consistency regularizer jointly improve the localization accuracy and measurement quality for each frame.
- **We develop the TT as a causal reliability-aware filter-predictor to close the tracking loop under bad frames.** Using the per-frame tokens from PAST, TT performs reliability-injected masked attention over a sliding window and outputs a filtered state and a one-step prediction, where the prediction directly initializes the next-frame probing beam under the same FF DFT codebook. An increment descriptor and a temporal physics loop further mitigate error propagation under bad frames.
- **We evaluate the performance of PAST-TT compared with other representative methods.** We carry out ex-

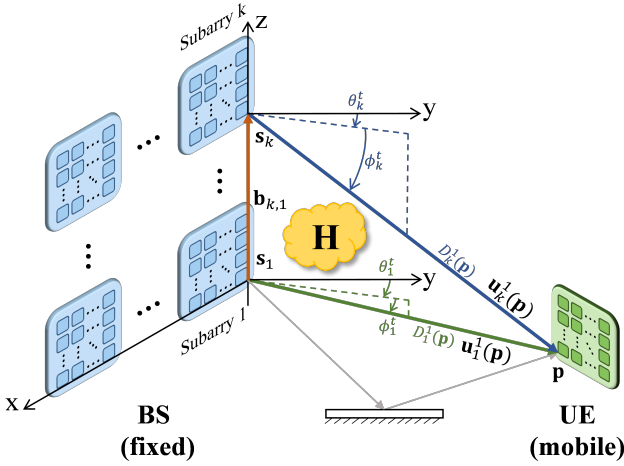


Fig. 1. THz UM-MIMO system model with fixed BS and mobile UE.

tensive simulations across SNRs, bad-frame rates and mobility. The results demonstrate that PAST-TT outperforms the compared solutions with improved estimation accuracy and robustness under intermittently corrupted observations, leading to higher spectral efficiency. Complexity analysis and GPU latency measurement further confirm that its critical-path latency at each frame stays below the frame interval and enables real-time tracking.

The remainder of this paper is organized as follows. Sec. II presents the system model with the parallax-aware NF channel and signal structure, and the problem formulation is also presented. Sec. III introduces PAST for per-frame localization and reliability-aware evidence extraction (an earlier version of the NF localization part was presented in [1]). Sec. IV develops the causal TT for online filtering and one-step prediction. Sec. V evaluates the performance of the proposed methods. Finally, Sec. VI concludes the paper.

II. SYSTEM OVERVIEW AND PROBLEM FORMULATION

In this section, we first introduce the system model of THz UM-MIMO, followed by the HSPM with parallax effects and the observation signal structure. Then, we formulate the per-frame localization and online beam tracking problems.

A. System Model

As illustrated in Fig. 1, we consider a THz downlink UM-MIMO system where a base station (BS) with widely-spaced subarrays serves a user equipment (UE) in the radiative NF region. The enlarged inter-subarray spacing not only improves the spatial multiplexing capability, but more critically, amplifies the geometric parallax effect that the same UE position induces distinct propagation distances and angles across subarrays. Specifically, the BS employs N_t transmit antennas designed as K uniform planar arrays (UPAs) on the x - z plane. Each subarray contains $N_s = N_t/K$ antennas with inter-element spacing $d = \lambda/2$ at central carrier wavelength λ , and the inter-subarray spacing is much larger than d . The UE is equipped with a UPA of N_r antennas with spacing d .

To reduce the hardware overhead, both the BS and UE adopt HBF structure. The BS uses a sub-connected architecture with

$L_t = K$ RF chains [6], therefore, the analog precoder $\mathbf{F}_{\text{RF}} \in \mathbb{C}^{N_t \times L_t}$ takes a block-diagonal form as

$$\mathbf{F}_{\text{RF}} = \text{blkdiag}(\mathbf{f}_{\text{RF},1}, \mathbf{f}_{\text{RF},2}, \dots, \mathbf{f}_{\text{RF},K}), \quad (1)$$

where $\mathbf{f}_{\text{RF},k} \in \mathbb{C}^{N_s}$ denotes the analog precoding vector of the k^{th} subarray for $k = 1, \dots, K$. Since the analog precoder is implemented by phase shifters, each element in $\mathbf{f}_{\text{RF},k}$ satisfies the constant-modulus constraint $|\mathbf{f}_{\text{RF},k}(i)| = 1/\sqrt{N_s}$. At the UE, a fully-connected architecture is adopted, where each of the L_r RF chains is connected to all N_r antennas through phase shifters. The analog combiner $\mathbf{W}_{\text{RF}} \in \mathbb{C}^{N_r \times L_r}$ also obeys the constant-modulus constraint.

The system operates with orthogonal frequency division multiplexing (OFDM) using M subcarriers with spacing Δf . At the m^{th} subcarrier, the BS transmits an N_{st} -dimensional symbol vector $\mathbf{s}[m] \in \mathbb{C}^{N_{st}}$. It is first processed by a digital baseband precoder $\mathbf{F}_{\text{BB}}[m] \in \mathbb{C}^{L_t \times N_{st}}$ and then by the analog precoder \mathbf{F}_{RF} . After that, it is propagated through the wideband THz channel $\mathbf{H}[m] \in \mathbb{C}^{N_r \times N_t}$. The UE applies the analog combiner \mathbf{W}_{RF} and a digital combiner $\mathbf{W}_{\text{BB}}[m] \in \mathbb{C}^{L_r \times N_{sr}}$ to form the N_{sr} -dimensional baseband output as

$$\mathbf{y}[m] = \mathbf{W}_{\text{eq}}^{\text{H}}[m]\mathbf{H}[m]\mathbf{F}_{\text{eq}}[m]\mathbf{s}[m] + \mathbf{W}_{\text{eq}}^{\text{H}}[m]\mathbf{n}[m], \quad (2)$$

where $\mathbf{F}_{\text{eq}}[m] = \mathbf{F}_{\text{RF}}\mathbf{F}_{\text{BB}}[m] \in \mathbb{C}^{N_t \times N_{st}}$ and $\mathbf{W}_{\text{eq}}[m] = \mathbf{W}_{\text{RF}}\mathbf{W}_{\text{BB}}[m] \in \mathbb{C}^{N_r \times N_{sr}}$ represent the precoding and combining matrices, respectively, with $\|\mathbf{F}_{\text{eq}}[m]\|_F^2 = 1$ and $\|\mathbf{W}_{\text{eq}}[m]\|_F^2 = 1$, and $\mathbf{n}[m] \sim \mathcal{CN}(\mathbf{0}, \sigma_n^2 \mathbf{I}_{N_r})$ is the additive white Gaussian noise. Moreover, the symbol vector is normalized as $\mathbb{E}[\mathbf{s}[m]\mathbf{s}^{\text{H}}[m]] = \rho \mathbf{I}_{N_{st}}$, where ρ denotes the average transmit power per subcarrier. To satisfy the total power constraint P_t across all M subcarriers, we have $M\rho = P_t$.

During the pilot transmission stage for beam tracking, the above model specializes to a configuration that enables parallax extraction across subarrays which share a common local oscillator and baseband. We set $N_{st} = K$ and adopt an identity digital precoder $\mathbf{F}_{\text{BB}}[m] = \frac{1}{\sqrt{K}}\mathbf{I}_K$, so that each stream is mapped to one subarray, while all subarrays are excited simultaneously toward the UE. To ensure that the UE can resolve the individual observation from each subarray, we employ FDM pilots with disjoint subcarrier subsets $\{\mathcal{M}_k\}_{k=1}^K$, where only the k^{th} stream is active for $m \in \mathcal{M}_k$. Moreover, we adopt a comb-type allocation where each \mathcal{M}_k uniformly spans the entire bandwidth with effective spacing of $K\Delta f$ for the observed tones of each subarray. For pilot transmission, the analog beam $\mathbf{f}_{\text{RF},k}$ is selected from a standard far-field DFT codebook. Under this design, the received pilots across frequency and subarrays implicitly encode the parallax information used by the subsequent transformer-based modules.

B. Near-Field Channel and Signal Structure

For the considered THz UM-MIMO system, the Rayleigh distance $D_R = \frac{2(S_b + S_u)^2}{\lambda}$ significantly expands, where S_b and S_u denote the array apertures at the BS and UE, respectively. As a result, a typical UE operates in the NF, where a global PWM fails to capture the non-negligible wavefront curvature across widely separated subarrays, whereas a full SWM is computationally heavy. To balance accuracy and complexity,

we adopt the HSPM, approximating the wavefront as planar within each subarray and spherical between subarrays. The applicability conditions of HSPM are provided in [8], [9].

Within each subarray, for azimuth θ and elevation ϕ , the generic UPA steering vector in PWM can be represented as

$$\mathbf{a}_N(\psi_x, \psi_z) = \left[1 \ \dots \ e^{j\frac{2\pi}{\lambda}\psi_n} \ \dots \ e^{j\frac{2\pi}{\lambda}\psi_{N-1}} \right]^T, \quad (3)$$

where $\psi_n = d_{n_x}\psi_x + d_{n_z}\psi_z$, $\psi_x = \sin\theta \cos\phi$ and $\psi_z = \sin\phi$. Here N is the number of elements in the subarray, (d_{n_x}, d_{n_z}) denotes the distances from the n^{th} antenna to the reference antenna on the x- and z-axis. With N_ℓ paths between the BS and the UE, the receive and transmit steering vectors of the k^{th} subarray for the ℓ^{th} path are denoted by $\mathbf{a}_k^{r\ell} = \mathbf{a}_{N_r}(\psi_{k_x}^{r\ell}, \psi_{k_z}^{r\ell})$ and $\mathbf{a}_k^{t\ell} = \mathbf{a}_{N_s}(\psi_{k_x}^{t\ell}, \psi_{k_z}^{t\ell})$, respectively. For the LoS path in Fig. 1, the distance $D_k^1(\mathbf{p})$ and direction vector $\mathbf{u}_k^1(\mathbf{p})$ from the k^{th} subarray (with reference position $\mathbf{s}_k = [x_k, 0, z_k]^T$) to the UE (at $\mathbf{p} = [x, y, z]^T$) are expressed as

$$D_k^1(\mathbf{p}) = \|\mathbf{p} - \mathbf{s}_k\|, \quad (4a)$$

$$\mathbf{u}_k^1(\mathbf{p}) = \frac{\mathbf{p} - \mathbf{s}_k}{D_k^1(\mathbf{p})} = [u_{k,x}, u_{k,y}, u_{k,z}]^T, \quad (4b)$$

In addition, the azimuth θ_k^t and elevation ϕ_k^t in the NF are uniquely determined by the specific geometry between \mathbf{p} and \mathbf{s}_k , following $\cos\theta_k^t = \frac{x-x_k}{D_k^1(\mathbf{p})\cos\phi_k^t}$ and $\sin\phi_k^t = \frac{z-z_k}{D_k^1(\mathbf{p})}$.

However, across the widely separated subarrays, the spherical wavefront curvature is non-negligible and induces distinct phase shifts corresponding to the varying distances. Combining the PWM within subarrays and the SWM across subarrays, the frequency-domain subchannel $\mathbf{H}_k[m] \in \mathbb{C}^{N_r \times N_s}$ between the k^{th} subarray and the UE at subcarrier f_m is modeled as

$$\mathbf{H}_k[m] = \sum_{\ell=1}^{N_\ell} \alpha_k^\ell e^{-j2\pi f_m \frac{D_k^\ell(\mathbf{p})}{c}} \mathbf{a}_k^{r\ell}(\mathbf{p}) (\mathbf{a}_k^{t\ell}(\mathbf{p}))^T, \quad (5)$$

where α_k^ℓ is the complex path gain and $D_k^\ell(\mathbf{p})$ is the path length of the ℓ^{th} path for the k^{th} subarray. The aggregate wideband channel is obtained by concatenation as $\mathbf{H}[m] = [\mathbf{H}_1[m], \dots, \mathbf{H}_K[m]] \in \mathbb{C}^{N_r \times N_t}$, and the FDM pilot scheme in Sec. II-A determines which subcarriers probe each $\mathbf{H}_k[m]$.

The enlarged inter-subarray spacing amplifies the geometric parallax. Taking the first subarray as the reference and defining the geo-arm vector $\mathbf{b}_{k,1} = \mathbf{s}_k - \mathbf{s}_1$, the geometry satisfies

$$D_k(\mathbf{p}) = \sqrt{D_1^2(\mathbf{p}) + \|\mathbf{b}_{k,1}\|^2 - 2D_1(\mathbf{p})(\mathbf{u}_1(\mathbf{p}) \cdot \mathbf{b}_{k,1})}, \quad (6a)$$

$$\mathbf{u}_k(\mathbf{p}) = \frac{D_1(\mathbf{p})\mathbf{u}_1(\mathbf{p}) - \mathbf{b}_{k,1}}{D_k(\mathbf{p})}, \quad (6b)$$

which reveals that the set $\{D_k(\mathbf{p}), \mathbf{u}_k(\mathbf{p})\}_{k=1}^K$ forms a geometry-consistent fingerprint of the UE position. In particular, the inter-subarray Time Difference of Arrival (TDoA) $\Delta\tau_{k,1} = (D_k - D_1)/c$ and the power fingerprints reflecting path-loss variations jointly encode the UE position. Comb-FDM induces a delay periodicity $T_{\text{amb}} = 1/(K\Delta f)$ in τ_k , but $\Delta\tau_{k,1}$ is ambiguity-free since $|\Delta\tau_{k,1}| \leq d_{\text{max}}/c < T_{\text{amb}}/2$.

When the UE moves, the channel parameters evolve over time $t = qT_0$, where $q \geq 1$ is the frame index and T_0 is the frame duration designed within the channel coherence time.

Under the comb-type FDM pilot design, the pilot symbol vector on the m^{th} subcarrier at the q^{th} frame is denoted as

$$\mathbf{s}[m, q] = \begin{cases} s_p[m, q] \mathbf{e}_k, & m \in \mathcal{M}_k, \\ \mathbf{0}, & \text{otherwise,} \end{cases} \quad (7)$$

where \mathbf{e}_k is the k^{th} canonical basis vector and $s_p[m, q]$ is a known pilot symbol with $\mathbb{E}\{|s_p[m, q]|^2\} = K\rho$. Exploiting $\mathbf{F}_{\text{BB}}[m] = \frac{1}{\sqrt{K}}\mathbf{I}_K$ and the block-diagonal structure of \mathbf{F}_{RF} , the scalar observation on the k^{th} stream is expressed as

$$y_k[m, q] = \mathbf{w}_{eq,k}^H[m] \mathbf{H}_k[m, q] \mathbf{f}_{\text{RF},k} \frac{1}{\sqrt{K}} s_p[m, q] + n_k[m, q], \quad (8)$$

where $\mathbf{w}_{eq,k}[m]$ is the effective combining vector used to extract the k^{th} pilot stream, and $n_k[m, q]$ is the post-combining noise. For LoS-dominant THz links and narrow pilot beams, the expression of (8) can be well approximated as

$$y_k[m, q] \approx \beta_k[m, q] e^{-j\Phi_k(m, q)} + n_k[m, q], \quad (9)$$

where $\beta_k[m, q]$ collects path loss, beamforming gain and pilot amplitude, and is slowly varying over frequency and frames. The phase admits a frequency-linear decomposition as

$$\Phi_k(m, q) = 2\pi f_m \tau_k(q) + \phi_{\text{ce}}(q) - \vartheta_k(q) + \epsilon_k[m, q], \quad (10)$$

where $\tau_k(q) = D_k^1(\mathbf{p}(q))/c$ is the propagation delay, $\phi_{\text{ce}}(q)$ is the common phase error (CPE) and $\vartheta_k(q) = 2\pi \sum_{i=0}^{q-1} \nu_k(i) T_0$ is the Doppler-induced accumulated phase with the instantaneous Doppler shift $\nu_k(q) = \frac{f_c}{c} \mathbf{v}^T(q) \mathbf{u}_k(\mathbf{p}(q))$. Residual mismatch is collected in $\epsilon_k[m, q]$, including weak multipath, beam-squint effects and other model misalignment to be handled in the subsequent uncertainty-aware learning framework.

Although $\Phi_k(m, q)$ is linear with f_m for fixed q , its evolution over q is nonlinear due to time-varying Doppler and motion. For robust beam tracking, we consider the inter-frame phase increment computed from $y_k^*[m, q] y_k[m, q-1]$, yielding

$$\begin{aligned} \Delta\Phi_k(m, q) &= \Phi_k(m, q) - \Phi_k(m, q-1), \\ &= 2\pi f_m \Delta\tau_k(q) - 2\pi \bar{\nu}_k(q) T_0 \\ &\quad + \Delta\phi_{\text{ce}}(q) + \Delta\epsilon_k[m, q], \end{aligned} \quad (11)$$

where $\Delta\tau_k(q)$, $\Delta\phi_{\text{ce}}(q)$ and $\Delta\epsilon_k[m, q]$ denote the corresponding variations over the q^{th} frame interval, and $\bar{\nu}_k(q)$ is the average Doppler over the q^{th} frame.

In summary, both $\Phi_k(m, q)$ and $\Delta\Phi_k(m, q)$ are affine in f_m , with slopes governed by $\tau_k(q)$ or $\Delta\tau_k(q)$. Across subarrays, the geometric parallax constraints in (6) tightly couple these parameters through the UE position. Therefore, the collection of frequency-linear signatures $\{\Phi_k(m, q)\}_{k,m}$ and their increments form a geometry-consistent fingerprint of the UE. Over time, the evolution of their slopes and offsets reflects the UE dynamics. This space-frequency-time structure provides the physical foundation of our work.

C. Problem Formulation

1) *Static Parallax-Aware Localization*: We first focus on a single frame and omit its frame index for brevity. Under the comb-type FDM pilot design, stacking all pilot observations across the K subarrays and their assigned subcarrier

subsets $\{\mathcal{M}_k\}_{k=1}^K$ yields $\mathbf{y} = [\{y_k[m]\}_{m \in \mathcal{M}_k, k=1}^K]^T \in \mathbb{C}^M$. Combining the HSPM channel in (5), the parallax constraints in (6) and the scalar phase structure in (9)-(10), \mathbf{y} follows the nonlinear parametric model as

$$\mathbf{y} = \mathbf{h}(\mathbf{p}, \boldsymbol{\eta}) + \mathbf{n}, \quad \mathbf{n} \sim \mathcal{CN}(\mathbf{0}, \sigma_n^2 \mathbf{I}_M), \quad (12)$$

where $\boldsymbol{\eta}$ collects nuisance parameters such as complex gains, beamforming gains and CPE. The maximum-likelihood (ML) estimator serves as a natural baseline, given by

$$\hat{\mathbf{p}}_{\text{ML}} = \arg \min_{\mathbf{p} \in \mathcal{P}} \min_{\boldsymbol{\eta}} \|\mathbf{y} - \mathbf{h}(\mathbf{p}, \boldsymbol{\eta})\|_2^2, \quad (13)$$

where \mathcal{P} is the BS coverage area. Due to the hybrid spherical-planar wavefront, inter-subarray parallax coupling and wide-band comb-type sampling, (13) is highly non-convex and high-dimensional, making direct ML search unsuitable for low-latency beam alignment. We therefore use PAST as a learned surrogate of the intractable ML estimator. For each frame, it maps the raw observation \mathbf{y} to a compact evidence packet as

$$\mathcal{E} = f_{\Theta_s}(\mathbf{y}), \quad (14)$$

which comprises a position estimate $\hat{\mathbf{p}}$, and parallax-aware evidence tokens extracted from the frequency-linear signatures, together with reliability indicators to quantify the frame-wise measurement quality. By design, \mathcal{E} preserves the geometry-informative content of (12) while reducing the per-frame input dimension for temporal tracking.

2) *Dynamic Beam Tracking*: To capture mobility, we define the kinematic state $\mathbf{x}(q) = [\mathbf{p}(q) \ \mathbf{v}(q)]^T \in \mathbb{R}^6$ and adopt a constant-velocity evolution model, given by

$$\mathbf{x}(q+1) = \mathbf{F}\mathbf{x}(q) + \mathbf{w}(q), \quad \mathbf{w}(q) \sim \mathcal{N}(\mathbf{0}, \mathbf{Q}), \quad (15)$$

where \mathbf{F} is determined by T_0 and \mathbf{Q} captures unmodeled accelerations. At the q^{th} frame, stacking the FDM pilot observations yields the observation model $\mathbf{y}(q) = \mathbf{h}_q(\mathbf{x}(q)) + \mathbf{n}(q)$ with $\mathbf{n}(q) \sim \mathcal{CN}(\mathbf{0}, \sigma_n^2 \mathbf{I}_M)$. Here, $\mathbf{h}_q(\cdot)$ encapsulates the delay, Doppler shift, the comb-type FDM sampling pattern and slowly varying gains. Equivalently, through (10) and (11), each subarray provides a frequency-affine phase signature whose slope and intercept evolve with $\mathbf{x}(q)$ under the geometric parallax, while residual mismatch is modeled as a disturbance.

The beam tracking task is to recursively infer $\mathbf{x}(q)$ from $\mathbf{y}(0:q)$. The Bayes-optimal solution would propagate the filtering posterior $p(\mathbf{x}(q) | \mathbf{y}(0:q))$ under (15) and the observation model, but exact nonlinear filtering is analytically intractable and can be computationally expensive for high-dimensional observations. Therefore, to obtain a low-latency and robust learned tracker, we adopt a cascaded formulation as

$$\mathcal{E}(q) = f_{\Theta_s}(\mathbf{y}(q)), \quad \hat{\mathbf{x}}(q) = f_{\Theta_T}(\mathcal{E}(0), \dots, \mathcal{E}(q)), \quad (16)$$

where the TT $f_{\Theta_T}(\cdot)$ acts as a learned nonlinear filter-predictor operating on the compact evidence sequence.

This design mirrors the classical separation between measurement processing and state estimation, leveraging physics-structured tokenization and spatial-temporal attention rather than black-box modeling. Importantly, using $\mathcal{E}(q)$ avoids a monolithic spatial-temporal network over raw pilots, improving sample efficiency and reducing runtime while preserving geometry-informative signatures for tracking.

III. PAST FOR STATIC LOCALIZATION

In this section, we introduce the PAST, which leverages a deep neural network to extract and interpret the rich NF parallax signatures from lightweight FF codebook excitations, bypassing the need for prohibitive NF beam sweeping.

A. Feature Distillation and Physical Tokenization

PAST takes the received comb-type FDM pilots as input and serves as a physics-informed measurement encoder. It distills geometry-informative evidence consistent with the channel model, parallax constraints, and the per-frame frequency-affine phase structure. Specifically, it compresses the high-dimensional FDM measurements into reliability-aware physical tokens, which are fused into a compact evidence packet \mathcal{E} for the downstream TT. The pipeline below is defined for a single frame with its index omitted. We sort $\mathcal{M}_k = \{m_{k,1}, \dots, m_{k,L_k}\}$ and define $y_{k,i} = y_k[m_{k,i}]$ and $f_{k,i} = f_{m_{k,i}}$ for $i = 1, \dots, L_k$.

To obtain stable phase-increment signatures with bounded token length and prevent unreliable patches from contaminating the wideband evidence, we partition $\{1, \dots, L_k\}$ into G disjoint contiguous groups $\{\mathcal{I}_{k,g}\}_{g=1}^G$. The group energy is $E_{k,g} = \sum_{i \in \mathcal{I}_{k,g}} |y_{k,i}|^2$, and the normalized power weight for $i \in \mathcal{I}_{k,g}$ is $w_{k,g}[i] = \frac{|y_{k,i}|^2 + \varepsilon}{\sum_{j \in \mathcal{I}_{k,g}} (|y_{k,j}|^2 + \varepsilon)}$, where $\varepsilon > 0$ is a small constant. After that, the weighted frequency centroid $\bar{f}_{k,g}$ and spread $\sigma_{k,g}^2$ are represented as

$$\bar{f}_{k,g} = \sum_{i \in \mathcal{I}_{k,g}} w_{k,g}[i] f_{k,i}, \quad (17a)$$

$$\sigma_{k,g}^2 = \sum_{i \in \mathcal{I}_{k,g}} w_{k,g}[i] (f_{k,i} - \bar{f}_{k,g})^2. \quad (17b)$$

Since the Fisher information of τ_k scales with the power-weighted second central frequency moment, $(E_{k,g}, \sigma_{k,g}^2)$ are physics-grounded descriptors of groupwise delay information.

To exploit the frequency-affine structure without fragile phase unwrapping, we form adjacent-tone products. Defining $\mathcal{I}_{k,g}^\Delta = \{i \in \mathcal{I}_{k,g} : i+1 \in \mathcal{I}_{k,g}\}$ and $r_{k,i} = y_{k,i+1} y_{k,i}^*$ for $i \in \mathcal{I}_{k,g}^\Delta$, under (9)-(10), we can derive

$$-\angle r_{k,i} = \Phi_k(f_{k,i+1}) - \Phi_k(f_{k,i}) + \Delta\epsilon_k, \quad (18)$$

where the dominant term is the delay-induced increment $2\pi(f_{k,i+1} - f_{k,i})\tau_k$, while frequency-flat phase offsets within a frame are suppressed by differencing. The remaining perturbations are absorbed into $\Delta\epsilon_k$ and reflected in the reliability score. After that, with $u_{k,i} = r_{k,i}/|r_{k,i}|$, the magnitude-weighted circular mean is expressed as

$$\bar{u}_{k,g} = \frac{\sum_{i \in \mathcal{I}_{k,g}^\Delta} |r_{k,i}| u_{k,i}}{\sum_{i \in \mathcal{I}_{k,g}^\Delta} |r_{k,i}|}. \quad (19)$$

The reliability score and wrapped slope are defined as $\kappa_{k,g} = |\bar{u}_{k,g}| \in [0, 1]$ (higher $\kappa_{k,g}$ indicates a more consistent patch) and $\varphi_{k,g} = -\angle(\bar{u}_{k,g})$, respectively. Since $\varphi_{k,g}$ is wrapped under the comb spacing, it is embedded continuously with

$$\mathbf{q}_{k,g} = \begin{bmatrix} \cos \varphi_{k,g} \\ \sin \varphi_{k,g} \end{bmatrix} = \frac{1}{|\bar{u}_{k,g}| + \varepsilon} \begin{bmatrix} \Re\{\bar{u}_{k,g}\} \\ -\Im\{\bar{u}_{k,g}\} \end{bmatrix}. \quad (20)$$

Any remaining wrapping ambiguity is handled in the subsequent attention layers by parallax consistency, cross-group evidence and reliability scores, rather than explicit unwrapping.

For each subarray-group pair (k, g) , a compact descriptor is represented as

$$\mathbf{t}_{k,g} = [\log(E_{k,g} + \varepsilon), \log(\sigma_{k,g}^2 + \varepsilon), \mathbf{q}_{k,g}^T, \kappa_{k,g}]^T \in \mathbb{R}^{d_t}. \quad (21)$$

Then it is mapped into the transformer latent space by

$$\mathbf{z}_{k,g} = \mathbf{W}_{emb} \mathbf{t}_{k,g} + \mathbf{e}_k + \mathbf{e}_{gr} + \mathbf{e}_b, \quad (22)$$

where \mathbf{W}_{emb} is learnable, \mathbf{e}_k and \mathbf{e}_{gr} encode the subarray and group indices, and the fixed geometry encoding \mathbf{e}_b is derived from (6). The resulting per-frame token sequence with length KG is denoted as

$$\mathbf{Z} = [\mathbf{z}_{1,1}, \dots, \mathbf{z}_{1,G}, \dots, \mathbf{z}_{K,1}, \dots, \mathbf{z}_{K,G}]. \quad (23)$$

This physics-driven tokenization preserves parallax evidence while suppressing nuisance variations in raw pilots, allowing the tracker to focus on filtering and prediction under the kinematic prior, rather than low level denoising and feature learning from high dimensional complex pilots.

B. Physics-Driven Attention Mechanism

For the token sequence \mathbf{Z} , PAST uses a physics-driven attention encoder to fuse multi-subarray and multi-band evidence into \mathcal{E} and $\hat{\mathbf{p}}$. The attention weights explicitly incorporate the geometry prior and token-wise reliability in Sec. III-A.

To quantify token-wise reliability for evidence fusion, a scalar gate $c_{k,g} \in [0, 1]$ for the pair (k, g) is defined as

$$c_{k,g} = \kappa_{k,g} \cdot \sigma\left(\gamma_0 + \gamma_1 \log(E_{k,g} + \varepsilon) + \gamma_2 \log(\sigma_{k,g}^2 + \varepsilon)\right), \quad (24)$$

where $\sigma(\cdot)$ is the sigmoid function and $\gamma_1, \gamma_2 \geq 0$ are learned scaling factors enforced by $\gamma_a = \log(1 + \exp(\tilde{\gamma}_a))$ for $a \in \{1, 2\}$. It preserves the physical monotonicity that higher usable energy and larger effective frequency spread increase the confidence, yielding a bounded gate for stable scaling and gradients. Accordingly, $c_{k,g}$ serves as a learned confidence score to steer attention toward informative and phase-consistent patches. Then, denoting the i^{th} element in (23) as \mathbf{z}_i , we form query, key and value projections $\mathbf{q}_i^{(h)} = \mathbf{W}_Q^{(h)} \mathbf{z}_i$, $\mathbf{k}_i^{(h)} = \mathbf{W}_K^{(h)} \mathbf{z}_i$ and $\mathbf{v}_i^{(h)} = \mathbf{W}_V^{(h)} \mathbf{z}_i$ in each attention head h . The attention logit from token i to token j is defined as

$$\ell_{ij}^{(h)} = \frac{(\mathbf{q}_i^{(h)})^T \mathbf{k}_j^{(h)}}{\sqrt{d_h}} + b_{ij}^{(h)} + \delta \log(c_{k(j),g(j)} + \varepsilon), \quad (25)$$

where d_h is the per-head dimension, $\delta \in [0, 1]$ balances source selection and content aggregation to avoid over-suppression, $k(\cdot)$ and $g(\cdot)$ map each token to its subarray and group indices. The observation-independent geometry bias $b_{ij}^{(h)}$ is injected as

$$b_{ij}^{(h)} = \text{MLP}_{\text{geo}}^{(h)}\left([\mathbf{b}_{k(i),k(j)}/\Lambda]^T, \Delta g_{ij}\right)^T, \quad (26)$$

where $\mathbf{b}_{k(i),k(j)} = \mathbf{b}_{k,k'}$ is the known geo-arm vector, $\Lambda = \sqrt{\frac{2}{K(K-1)} \sum_{1 \leq k < k' \leq K} \|\mathbf{b}_{k,k'}\|^2}$ normalizes geo-arm lengths, $\Delta g_{ij} = g(i) - g(j)$, and $\text{MLP}_{\text{geo}}^{(h)}(\cdot)$ is a lightweight Feed-forward network (FFN) mapping the relative-geometry

features to a scalar bias. The corresponding attention weight is $\alpha_{ij}^{(h)} = \text{softmax}_j(\ell_{ij}^{(h)})$, and the head output is given by

$$\mathbf{o}_i^{(h)} = \sum_j \alpha_{ij}^{(h)} (c_{k(j),g(j)})^{1-\delta} \mathbf{v}_j^{(h)}. \quad (27)$$

In (25) and (27), $\delta \log(c)$ controls competition among candidate evidence sources, while $c^{1-\delta}$ controls their contribution magnitude. Standard multi-head concatenation and an FFN then yield updated token representations.

Motivated by (10) that all frequency groups within one subarray share the same per-frame delay and the parallax consistency across subarrays, we factorize the encoder into an intra-subarray stage $\text{Enc}_{\text{intra}}(\cdot)$ and an inter-subarray stage $\text{Enc}_{\text{inter}}(\cdot)$, both using the attention in (25)-(27). First, $\text{Enc}_{\text{intra}}(\cdot)$ is applied to each $\mathbf{Z}_k = [\mathbf{z}_{k,1}, \dots, \mathbf{z}_{k,G}]$ to obtain $\tilde{\mathbf{z}}_k = [\tilde{\mathbf{z}}_{k,1}, \dots, \tilde{\mathbf{z}}_{k,G}]$, where $\text{Enc}_{\text{intra}}(\cdot)$ shares parameters across k . A reliability-aware pooling then produces a subarray summary token as

$$\bar{\mathbf{z}}_k = \sum_{g=1}^G \pi_{k,g} \tilde{\mathbf{z}}_{k,g}, \quad (28)$$

where $\pi_{k,g} = \text{softmax}_g(\mathbf{w}_P^T \tilde{\mathbf{z}}_{k,g} + \log(c_{k,g} + \varepsilon))$ and \mathbf{w}_P is the pooling vector. For inter-subarray gating, a subarray-level confidence score $\bar{c}_k = \sum_{g=1}^G \pi_{k,g} c_{k,g}$ replaces $c_{k(j),g(j)}$ in (25) and (27), and $\text{Enc}_{\text{inter}}(\cdot)$ is applied to $\mathbf{S} = [\mathbf{z}_0, \bar{\mathbf{z}}_1, \dots, \bar{\mathbf{z}}_K]$ with $\Delta g_{ij} = 0$. Here, \mathbf{z}_0 is the global token used to aggregate frame-level evidence, with $\bar{c}_0 = 1$ and $\mathbf{b}_{0,k} = \mathbf{b}_{k,0} = \mathbf{0}$.

The final spatial estimate is obtained by a lightweight head on the global token as

$$\hat{\mathbf{p}} = \mathbf{W}_p \mathbf{h}_0 + \mathbf{b}_p, \quad (29)$$

where \mathbf{h}_0 is the output of \mathbf{z}_0 after $\text{Enc}_{\text{inter}}(\cdot)$, and $\hat{r} = \sigma(\mathbf{w}_r^T \mathbf{h}_0 + b_r) \in (0, 1)$ is a compact quality indicator. After that, the per-frame evidence interface is denoted as

$$\mathcal{E} = [\hat{\mathbf{p}}, \mathbf{h}_0, \{\bar{\mathbf{z}}_k\}_{k=1}^K, \hat{r}], \quad (30)$$

where the fine-grained gates $\{c_{k,g}\}$ and pooling weights $\{\pi_{k,g}\}$ are auxiliary for diagnostics, and the factorized fusion reduces the dominant attention cost from $\mathcal{O}((KG)^2)$ to $\mathcal{O}(KG^2 + K^2)$ per frame.

C. Physics-in-the-Loop Training and Localization

PAST is trained as a low latency amortized solver for the ML inverse problem in (12), combining supervised localization and a physics-in-the-loop consistency regularizer. To complete the physics loop, we define a differentiable forward operator that predicts the token evidence from a candidate position \mathbf{p} , using the same ordered-comb indices $\{f_{k,i}\}$, adjacent set $\mathcal{I}_{k,g}^\Delta$ and magnitude weights proportional to $|r_{k,i}|$ as in Sec. III-A. For the k^{th} subarray with delay $\tau_k(\mathbf{p}) = \|\mathbf{p} - \mathbf{s}_k\|/c$, the corresponding ideal adjacent-tone phase increment is given by

$$\hat{r}_{k,i}(\mathbf{p}) = \exp(-j2\pi(f_{k,i+1} - f_{k,i})\tau_k(\mathbf{p})), \quad i \in \mathcal{I}_{k,g}^\Delta, \quad (31)$$

where $|\hat{r}_{k,i}(\mathbf{p})| = 1$. Replacing $u_{k,i}$ in (19) with $\hat{r}_{k,i}(\mathbf{p})$ yields the predicted group-wise circular mean $\hat{u}_{k,g}(\mathbf{p})$. Then, applying (20) to $\hat{u}_{k,g}(\mathbf{p})$ gives the predicted wrapped-slope

Algorithm 1 PAST: Per-Frame Inference and Physics-in-the-Loop Training.

- 1: **Input:** Pilots $\{y_k[m]\}_{m \in \mathcal{M}_k, k=1}^K$, subcarriers $\{f_m\}$, geolocations $\{\mathbf{b}_{k,1}\}$, partition $\{\mathcal{Z}_{k,g}\}_{g=1}^G$, parameters Θ_S .
 - 2: **Output:** $\mathcal{E} = [\hat{\mathbf{p}}, \mathbf{h}_0, \{\bar{\mathbf{z}}_k\}_{k=1}^K, \hat{r}]$.
 - 3:
 - 4: INFER-PAST($\{y_k[m]\}; \Theta_S$)
 - 5: **for** $k = 1$ **to** K **do**
 - 6: Construct $\mathbf{Z}_k = \{\mathbf{z}_{k,g}\}_{g=1}^G$ and $\{c_{k,g}\}_{g=1}^G$ via (17)-(24) (including $(\mathbf{q}_{k,g}, \kappa_{k,g})$ in (20)).
 - 7: $\bar{\mathbf{Z}}_k \leftarrow \text{Enc}_{\text{intra}}(\mathbf{Z}_k)$ using (25)-(27).
 - 8: Obtain view token $\bar{\mathbf{z}}_k$ and confidence \bar{c}_k via (28).
 - 9: **end for**
 - 10: Form $\mathbf{S} = [\mathbf{z}_0, \bar{\mathbf{z}}_1, \dots, \bar{\mathbf{z}}_K]$ with $\bar{c}_0 = 1$, and compute $\tilde{\mathbf{S}} \leftarrow \text{Enc}_{\text{inter}}(\mathbf{S})$ using (25)-(27).
 - 11: Read out \mathbf{h}_0 and predict $(\hat{\mathbf{p}}, \hat{r})$ by (29); **return** \mathcal{E} .
 - 12:
 - 13: TRAIN-PAST($\{(y_n, \mathbf{p}_n)\}; \Theta_S$)
 - 14: Run INFER-PAST; compute \mathcal{L}_{sup} by (32) and $\mathcal{L}_{\text{phy}}^s$ by (31)-(33).
 - 15: Update Θ_S by minimizing \mathcal{L}_S in (34).
-

embedding $\hat{\mathbf{q}}_{k,g}(\mathbf{p})$, and we define the forward map as $\mathcal{F}_{k,g}(\mathbf{p}) = \hat{\mathbf{q}}_{k,g}(\mathbf{p})$.

To improve robustness to bad frames, we map the quality indicator \hat{r} in (29) to a log-variance $s = \log \hat{\sigma}_p^2 = \log \frac{1-\hat{r}+\varepsilon}{\hat{r}+\varepsilon}$ in a heteroscedastic regression form, and $\hat{\sigma}_p^2 = e^s$ represents an input-dependent uncertainty of the position regression. For numerical stability, we clip s to a bounded interval and use the Gaussian negative log-likelihood, given by

$$\mathcal{L}_{\text{sup}} = \exp(-s) \|\hat{\mathbf{p}} - \mathbf{p}\|_2^2 + s. \quad (32)$$

To enforce physical consistency, we regularize the embedding $\mathbf{q}_{k,g}$ toward the forward prediction $\mathcal{F}_{k,g}(\hat{\mathbf{p}})$, using $c_{k,g}$ in (24) as a learned precision proxy. With the wrap-safe similarity $d(\mathbf{a}, \mathbf{b}) = 1 - \mathbf{a}^T \mathbf{b}$ for normalized embeddings, we define

$$\mathcal{L}_{\text{phy}}^s = \sum_{k=1}^K \sum_{g=1}^G \frac{\text{sg}(c_{k,g})}{\frac{1}{KG} \sum_{k',g'} \text{sg}(c_{k',g'})} \varpi \left(d(\mathbf{q}_{k,g}, \mathcal{F}_{k,g}(\hat{\mathbf{p}})) \right), \quad (33)$$

where $\varpi(\cdot)$ is a smooth robust penalty like Charbonnier and $\text{sg}(\cdot)$ stops gradients to avoid trivially reducing $\mathcal{L}_{\text{phy}}^s$ by shrinking the gates. The overall training objective is

$$\mathcal{L}_S = \mathcal{L}_{\text{sup}} + \lambda_{\text{phy}}^s \mathcal{L}_{\text{phy}}^s, \quad (34)$$

where λ_{phy}^s is annealed from 0 to its target value to stabilize early training, and weight decay is applied in the optimizer.

PAST outputs the per-frame estimate $\hat{\mathbf{p}}$ together with a compact uncertainty indicator, forming a reliability-aware measurement interface to the downstream temporal tracker. The algorithm of PAST is summarized in Algorithm 1.

IV. TEMPORAL TRANSFORMER FOR TRACKING

In this section, we introduce the causal TT that turns per-frame PAST evidence into reliability-aware tracking, jointly performing filtering and prediction under a physics loop, as shown in Fig. 2.

A. Frame-Level Design and Motion Model

We adopt the frame interval T_0 defined in Sec. II-B and the effective pilot duration $T_p \ll T_0$. Specifically, T_p is designed to satisfy the frame-wise quasi-static condition $2\pi f_{D,\text{max}} T_p \leq \epsilon_p$, where $f_{D,\text{max}} = v_{\text{max}}/\lambda$ is the maximum Doppler shift induced by the largest UE velocity v_{max} , and ϵ_p bounds the intra-pilot phase rotation, ensuring the extracted evidence $\mathcal{E}(q)$ can be treated as a single state-space measurement. Moreover, the tracking update period T_0 is selected from a directional beam-coherence viewpoint to keep the evolution of the NF evidence between frames locally smooth. Two drift budgets, $\omega_{\text{max}} T_0 \leq \rho_\theta \Theta$ and $\Delta\tau_{\text{max}} \leq \rho_\tau/B$, are imposed, where Θ is the half-power beamwidth of the analog beam, B is the bandwidth and $\rho_\theta, \rho_\tau \in (0, 1)$ are dimensionless margins. The angular rate ω is upper bounded by $\omega_{\text{max}} \leq v_{\perp,\text{max}}/r_{\text{min}}$, where $v_{\perp,\text{max}}$ is the maximum transverse speed and r_{min} is the minimum distance between BS and UE. For delay drift, with $\tau_k(q)$ denoting the LoS propagation delay of the k^{th} subarray at the q^{th} frame, a sufficient condition is $|\tau_k(q) - \tau_k(q-1)| \leq v_{r,\text{max}} T_0/c$ for all k , hence $v_{r,\text{max}} T_0/c \leq \rho_\tau/B$ ensures $\Delta\tau_{\text{max}} \leq \rho_\tau/B$.

Following Sec. II-C, we adopt the kinematic prior with T_0 , and set the state transition matrix in (15) as

$$\mathbf{F} = \begin{bmatrix} \mathbf{I}_3 & T_0 \mathbf{I}_3 \\ \mathbf{0} & \mathbf{I}_3 \end{bmatrix}, \quad (35)$$

which induces a locally smooth propagation over one update while leaving inter-frame maneuvers to be absorbed by the downstream learnable module. For reproducibility, the process-noise covariance is parameterized by the standard integrated acceleration form with strength $q_a \geq 0$, given by

$$\mathbf{Q} = q_a \begin{bmatrix} \frac{T_0^4}{4} \mathbf{I}_3 & \frac{T_0^3}{2} \mathbf{I}_3 \\ \frac{T_0^3}{2} \mathbf{I}_3 & T_0^2 \mathbf{I}_3 \end{bmatrix}, \quad (36)$$

where q_a controls the departure from the locally smooth prior, acting as a lightweight regularizer rather than a hard motion law, and a larger q_a admits stronger inter-frame deviations. The same form applies to planar tracking by replacing \mathbf{I}_3 with \mathbf{I}_2 .

B. Input Sequence and Tokenization

Following the per-frame interface in (30), we index the evidence from PAST at the q^{th} frame as

$$\mathcal{E}(q) = [\hat{\mathbf{p}}(q), \mathbf{h}_0(q), \{\bar{\mathbf{z}}_k(q)\}_{k=1}^K, \hat{r}(q)], \quad (37)$$

where $\bar{\mathbf{z}}_k(q)$ is the view token from the k^{th} subarray with parallax effect and $\hat{r}(q) \in (0, 1)$ is the quality indicator of each frame. Beyond the static evidence in $\mathcal{E}(q)$, inspired by the signal structure in (10) and (11), a slope-offset proxy via a circular least-squares fit on the unit circle is defined as

$$\begin{aligned} (\widehat{\Delta\tau}_k(q), \widehat{\zeta}_k(q)) = \\ \arg \min_{\Delta\tau, \zeta} \sum_{m \in \mathcal{M}_k} w_{k,m}(q) \left| e^{j\Delta\Phi_k(m,q)} - e^{j(2\pi f_m \Delta\tau - \zeta)} \right|^2, \end{aligned} \quad (38)$$

where $w_{k,m}$ is the normalized weight based on magnitude with $\sum_{m \in \mathcal{M}_k} w_{k,m}(q) = 1$. To suppress common-mode offsets shared across subarrays, we have $\widehat{\zeta}_k^{\text{rel}}(q) = \widehat{\zeta}_k(q) - \widehat{\zeta}_1(q)$

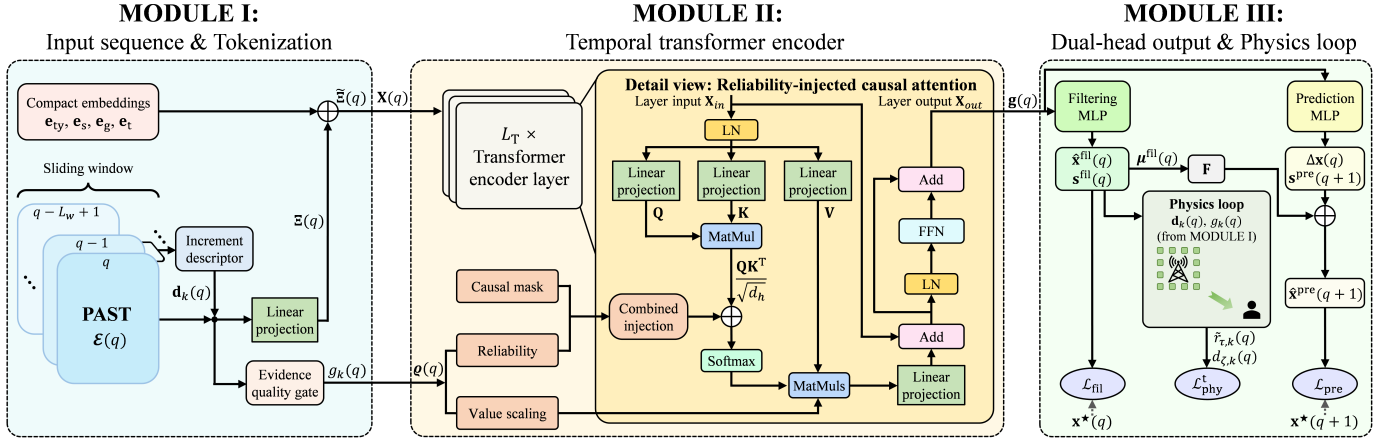


Fig. 2. Temporal transformer.

for $k \geq 2$ and $\hat{\zeta}_1^{\text{rel}}(q) = 0$. To enable explicit detection of unreliable inter-frame increments without phase unwrapping, the residual-consistency score is defined as

$$\kappa_k^\Delta(q) = \left| \sum_{m \in \mathcal{M}_k} w_{k,m}(q) e^{j(\Delta\Phi_k(m,q) - 2\pi f_m \widehat{\Delta}\tau_k(q) + \hat{\zeta}_k(q))} \right|. \quad (39)$$

For each subarray, we form a compact increment descriptor as

$$\mathbf{d}_k(q) = \left[\frac{c}{T_0} \widehat{\Delta}\tau_k(q), \cos(\hat{\zeta}_k^{\text{rel}}(q)), \sin(\hat{\zeta}_k^{\text{rel}}(q)), \kappa_k^\Delta(q) \right]^T. \quad (40)$$

For initialization, we set $\mathbf{d}_k(0) = \mathbf{0}$.

To preserve cross-subarray contrasts, we form a structured token list with $1+K$ tokens per frame as

$$\Xi(q) = [\xi_0(q), \xi_1(q), \dots, \xi_K(q)] \in \mathbb{R}^{(K+1) \times d_T}, \quad (41)$$

where the global token $\xi_0(q)$ and other $\xi_k(q)$ are mapped to a d_T -dimensional space via shared linear projections, given by

$$\xi_0(q) = \mathbf{W}_0 [\mathbf{h}_0^T(q), \hat{\mathbf{p}}^T(q), \hat{r}(q)]^T + \mathbf{b}_0, \quad (42a)$$

$$\xi_k(q) = \mathbf{W}_1 [\mathbf{z}_k^T(q), \mathbf{d}_k^T(q)]^T + \mathbf{b}_1, \quad (42b)$$

where $\mathbf{W}_0, \mathbf{W}_1$ and $\mathbf{b}_0, \mathbf{b}_1$ are learnable and shared across frames. This token grammar supports cross-view comparison and temporal linking for attention and injects physically grounded temporal drift cues via $\mathbf{d}_k(q)$ without exposing raw pilots to TT. To encode the subarray structure while keeping the temporal encoder generic, four compact embeddings are added: token type, subarray identity, geo-arm and temporal encoding. For $k = 0, \dots, K$, we define

$$\tilde{\xi}_k(q) = \xi_k(q) + \mathbf{e}_{\text{ty}}(\eta(k)) + \mathbf{e}_s(k) + \mathbf{e}_g(k) + \mathbf{e}_t(q), \quad (43)$$

where $\eta(0) = 0$, $\mathbf{e}_g(0) = \mathbf{0}$, and for $k \geq 1$, $\eta(k) = 1$ with the geometry anchor $\mathbf{e}_g(k) = \text{MLP}_b(\mathbf{b}_{k,1}/\Lambda)$ computed from the known geo-arm vectors. Here, $\text{MLP}_b(\cdot)$ is a two-layer perceptron with ReLU nonlinearity, output dimension d_T and a hidden width $\lfloor d_T/2 \rfloor$. In addition, $\mathbf{e}_{\text{ty}}(\cdot)$ and $\mathbf{e}_s(\cdot)$ are learnable, and $\mathbf{e}_t(q)$ is a standard temporal sinusoidal positional encoding. We then define a lightweight evidence-quality gate $g_k(q) = \sigma(a_0 + a_r \hat{r}(q) + a_\kappa \kappa_k^\Delta(q) + \mathbf{w}_g^T \xi_k(q)) \in (0, 1)$, and set $g_0(q) = 1$ for the global token and learnable parameters

$(a_0, a_r, a_\kappa, \mathbf{w}_g)$. It will be used in Sec. IV-C to form token reliability weights and bias masked attention without altering the token construction.

For online tracking, at the q^{th} frame, the most recent L_w evidence packets are collected to form the token tensor as

$$\underline{\mathbf{X}}(q) = [\tilde{\Xi}(q-L_w+1), \dots, \tilde{\Xi}(q)] \in \mathbb{R}^{L_w \times (K+1) \times d_T}, \quad (44)$$

where $\tilde{\Xi}(q) = [\tilde{\xi}_0(q), \dots, \tilde{\xi}_K(q)]$. To simplify the causal masking in Sec. IV-C, (44) is flattened into a token sequence with length $N = L_w(K+1)$ in a time-major order as

$$\mathbf{X}(q) = \text{Flatten}(\underline{\mathbf{X}}(q)), \quad (45)$$

with the index mapping $n \leftrightarrow (q'(n), k(n))$ for $n = 0, \dots, N-1$, where $q'(n) = q - L_w + 1 + \lfloor \frac{n}{K+1} \rfloor$, $k(n) = n \bmod (K+1)$, and $\mathbf{x}_n = \tilde{\xi}_{k(n)}(q'(n))$.

With N tokens per window, TT has an $\mathcal{O}(N^2)$ attention cost, independent of the subcarrier dimension due to the distilled interface in (37) and the increment descriptor in (40).

C. Causal Temporal Transformer Encoder

TT performs online causal sequence reasoning based on (45) through masked self-attention with an additive mask on the attention logits. Accordingly, evidence from future frames is excluded. For initialization when $q < L_w - 1$, tokens with $q'(n) < 0$ are padded with a padding token. We also define the validity indicator for the n^{th} token as $s_n(q) = 1$ for $q'(n) \geq 0$ and $s_n(q) = 0$ otherwise. Then, the additive mask matrix $\mathbf{M}(q) \in \mathbb{R}^{N \times N}$ is defined as

$$\mathbf{M}_{n,m}(q) = \begin{cases} 0, & s_m(q) = 1 \text{ and } s_n(q) = 0, \\ 0, & s_m(q) = s_n(q) = 1 \text{ and } q'(m) \leq q'(n), \\ -\infty, & \text{otherwise,} \end{cases} \quad (46)$$

This construction excludes padding tokens as keys or values ($s_m = 0$), prevents valid queries from attending to future frames ($q'(m) > q'(n)$) and allows bidirectional attention for tokens within each frame. The first case in (46) avoids an all- $-\infty$ mask row for padded queries, which would make the softmax ill-defined. These outputs are ignored at readout.

Each token \mathbf{x}_m in $\mathbf{X}(q)$ is associated with a reliability weight $\varrho_m(q) \in (0, 1]$, given by

$$\varrho_m(q) = \begin{cases} 1, & s_m(q) = 0, \\ 1, & s_m(q) = 1 \text{ and } k(m) = 0, \\ g_{k(m)}(q'(m)), & s_m(q) = 1 \text{ and } 1 \leq k(m) \leq K, \end{cases} \quad (47)$$

with $\boldsymbol{\varrho}(q) = [\varrho_0(q), \dots, \varrho_{N-1}(q)]^T$.

We set $\mathbf{H}^{(0)}(q) = \mathbf{X}(q)$ and employ L_T identical causal encoder blocks. For $\ell_t = 1, \dots, L_T$, the ℓ_t^{th} block follows the pre-normalization (Pre-LN) form as

$$\mathbf{H}^{(\ell_t)}(q) = \mathbf{H}^{(\ell_t-1)}(q) + \text{MSA}\left(\text{LN}(\mathbf{H}^{(\ell_t-1)}(q)); \mathbf{M}(q), \boldsymbol{\varrho}(q)\right), \quad (48a)$$

$$\mathbf{H}^{(\ell_t)}(q) = \mathbf{H}^{(\ell_t)}(q) + \text{FFN}\left(\text{LN}(\mathbf{H}^{(\ell_t)}(q))\right), \quad (48b)$$

where $\text{LN}(\cdot)$ is applied row-wise, and $\text{FFN}(\mathbf{z}) = \text{ReLU}(\mathbf{z}\mathbf{W}_1 + \mathbf{b}_1)\mathbf{W}_2 + \mathbf{b}_2$ is a two-layer position-wise FFN. Here, $\mathbf{W}_1 \in \mathbb{R}^{d_T \times d_T}$, $\mathbf{W}_2 \in \mathbb{R}^{d_T \times d_T}$, $d_T = 4d_{\text{T}}$ and $\mathbf{b}_1, \mathbf{b}_2$ are learnable. With N_h attention heads and $d_h = d_T/N_h$, for head h at layer ℓ_t , the standard projections are expressed as

$$\mathbf{Q}^{(\ell_t, h)} = \text{LN}(\mathbf{H}^{(\ell_t-1)})\mathbf{W}_Q^{(\ell_t, h)}, \quad (49a)$$

$$\mathbf{K}^{(\ell_t, h)} = \text{LN}(\mathbf{H}^{(\ell_t-1)})\mathbf{W}_K^{(\ell_t, h)}, \quad (49b)$$

$$\mathbf{V}^{(\ell_t, h)} = \text{LN}(\mathbf{H}^{(\ell_t-1)})\mathbf{W}_V^{(\ell_t, h)}, \quad (49c)$$

where $\mathbf{W}_Q^{(\ell_t, h)}, \mathbf{W}_K^{(\ell_t, h)}, \mathbf{W}_V^{(\ell_t, h)} \in \mathbb{R}^{d_T \times d_h}$ are learnable. The masked attention weights are then calculated as

$$\mathbf{A}^{(\ell_t, h)}(q) = \text{softmax}\left(\mathbf{Q}^{(\ell_t, h)}(\mathbf{K}^{(\ell_t, h)})^T / \sqrt{d_h} + \mathbf{M}(q) + \delta_T \mathbf{1} [\log(\boldsymbol{\varrho}(q) + \varepsilon)]^T\right), \quad (50)$$

where $\mathbf{1} \in \mathbb{R}^N$ is the all-one column vector, and $\text{softmax}(\cdot)$ is applied row-wise. The head output is computed as

$$\mathbf{O}^{(\ell_t, h)}(q) = \mathbf{A}^{(\ell_t, h)}(q) \left(\text{diag}(\boldsymbol{\varrho}(q))^{1-\delta_T} \mathbf{V}^{(\ell_t, h)}\right). \quad (51)$$

Therefore, TT injects $\boldsymbol{\varrho}(q)$ into attention competition and aggregation magnitude through the logit prior in (50) and value scaling in (51), explicitly downweighting tokens with low reliability. Finally, we obtain the multi-head output as

$$\text{MSA}(\mathbf{H}; \mathbf{M}, \boldsymbol{\varrho}) = [\mathbf{O}^{(\ell_t, 1)}(q), \dots, \mathbf{O}^{(\ell_t, N_h)}(q)]\mathbf{W}_O^{(\ell_t)}, \quad (52)$$

where $\mathbf{W}_O^{(\ell_t)} \in \mathbb{R}^{d_T \times d_T}$ is learnable. Under the time-major order in (45), the global token of the most recent frame has index $n_0(q) = (L_w - 1)(K + 1)$. Its final-layer representation $\mathbf{g}(q) = \mathbf{H}_{n_0(q)}^{(L_T)}(q) \in \mathbb{R}^{d_T}$ is used as the temporal summary.

D. Dual-Head Output and Physics Loop

Based on $\mathbf{g}(q)$, TT outputs a filtering estimate $\hat{\mathbf{x}}^{\text{fil}}(q)$ of the current kinematic state and a one-step prediction $\hat{\mathbf{x}}^{\text{pre}}(q+1)$ to initialize the beam tracking of the next frame. A differentiable physics loop further regularizes the outputs through NF geometry and drift-consistent increments.

The filtering head maps $\mathbf{g}(q)$ to a heteroscedastic Gaussian posterior proxy as

$$(\boldsymbol{\mu}^{\text{fil}}(q), \mathbf{s}^{\text{fil}}(q)) = f_{\text{fil}}(\mathbf{g}(q)), \quad (53)$$

where $\boldsymbol{\mu}^{\text{fil}}(q) = [\hat{\mathbf{p}}^{\text{fil}}(q) \hat{\mathbf{v}}^{\text{fil}}(q)]^T$, $\mathbf{s}^{\text{fil}}(q)$ is the log-variance vector and $\boldsymbol{\Sigma}^{\text{fil}}(q) = \text{diag}(\exp(\mathbf{s}^{\text{fil}}(q)))$. For prediction, we follow the kinematic prior and learn a residual correction as

$$(\Delta \mathbf{x}(q), \mathbf{s}^{\text{pre}}(q+1)) = f_{\text{pre}}(\mathbf{g}(q)), \quad (54a)$$

$$\boldsymbol{\mu}^{\text{pre}}(q+1) = \mathbf{F}\boldsymbol{\mu}^{\text{fil}}(q) + \Delta \mathbf{x}(q), \quad (54b)$$

where $\boldsymbol{\mu}^{\text{pre}}(q+1) = [\hat{\mathbf{p}}^{\text{pre}}(q+1) \hat{\mathbf{v}}^{\text{pre}}(q+1)]^T$, \mathbf{F} is given in (35) and $\boldsymbol{\Sigma}^{\text{pre}}(q+1) = \text{diag}(\exp(\mathbf{s}^{\text{pre}}(q+1)))$. With ground-truth $\mathbf{x}^*(q) = [\mathbf{p}^*(q) \mathbf{v}^*(q)]^T$, the filtering and prediction loss functions are defined as

$$\mathcal{L}_{\text{fil}} = \sum_q \left(\left\| \mathbf{x}^*(q) - \boldsymbol{\mu}^{\text{fil}}(q) \right\|_{(\boldsymbol{\Sigma}^{\text{fil}}(q))^{-1}}^2 + \log \det \boldsymbol{\Sigma}^{\text{fil}}(q) \right), \quad (55a)$$

$$\mathcal{L}_{\text{pre}} = \sum_q \left(\left\| \mathbf{x}^*(q+1) - \boldsymbol{\mu}^{\text{pre}}(q+1) \right\|_{(\boldsymbol{\Sigma}^{\text{pre}}(q+1))^{-1}}^2 + \log \det \boldsymbol{\Sigma}^{\text{pre}}(q+1) \right), \quad (55b)$$

which capture the robustness at the current frame and the forecasting capability at the next frame, respectively.

To suppress common-mode terms, we use the relative Doppler $\nu_k^{\text{rel}}(\mathbf{p}, \mathbf{v}) = \nu_k(\mathbf{p}, \mathbf{v}) - \nu_1(\mathbf{p}, \mathbf{v})$ for $k \geq 2$. Under the drift budgets in Sec. IV-A, the wrap-safe proxies $\widehat{\Delta\tau}_k(q)$ and $\widehat{\zeta}_k^{\text{rel}}(q)$ in (38) provide temporal cues with reliability, which are matched to the drift implied by the filtered state. We first define the normalized delay residual as

$$\tilde{r}_{\tau, k}(q) = \frac{\widehat{\Delta\tau}_k(q) - (\tau_k(\hat{\mathbf{p}}^{\text{fil}}(q)) - \tau_k(\hat{\mathbf{p}}^{\text{fil}}(q-1)))}{\Delta\tau_{\text{max}}}, \quad (56)$$

Then, the relative Doppler phase mismatch is modeled by

$$d_{\zeta, k}(q) = 1 - \cos(\widehat{\zeta}_k^{\text{rel}}(q) - 2\pi T_0 \nu_k^{\text{rel}}(\hat{\mathbf{p}}^{\text{fil}}(q), \hat{\mathbf{v}}^{\text{fil}}(q))), \quad (57)$$

which is invariant to 2π wrapping and acts as a mild consistency regularizer. Using $g_k(q)$ as a learned reliability proxy, we form a stop-gradient weight $\omega_k(q) = \frac{\text{sg}(g_k(q))}{\frac{1}{K} \sum_{k'=1}^K \text{sg}(g_{k'}(q))}$. In this way, the physics regularizer is obtained as

$$\mathcal{L}_{\text{phy}}^t = \sum_{q \geq 1} \left(\sum_{k=1}^K \omega_k(q) \varpi(\tilde{r}_{\tau, k}^2(q)) + \sum_{k=2}^K \omega_k(q) \varpi(2d_{\zeta, k}(q)) \right), \quad (58)$$

where $\varpi(\cdot)$ and $\text{sg}(\cdot)$ are the same as in (33). Finally, the TT training objective is expressed as

$$\mathcal{L}_T = \mathcal{L}_{\text{fil}} + \lambda_{\text{pre}} \mathcal{L}_{\text{pre}} + \lambda_{\text{phy}}^t \mathcal{L}_{\text{phy}}^t, \quad (59)$$

where λ_{phy}^t is annealed from 0 to its target value for stable early training.

V. PERFORMANCE EVALUATION

In this section, we evaluate the performance of the proposed PAST-TT framework for the considered THz NF scenario, and compare it with other representative methods.

A. Datasets and Simulation Setup

Under the system in Fig. 1, we generate both the static localization dataset for PAST and the sequential tracking dataset for TT with the simulation parameters in TABLE I. In this case, $S_b = 128\sqrt{10}\lambda$ and $S_u = \frac{3\sqrt{2}}{2}\lambda$, yielding a Rayleigh distance

TABLE I
SIMULATION PARAMETERS

Notation	Definition	Value
f_c	Carrier frequency	0.3 THz
B	Bandwidth	4 GHz
M	Number of subcarriers	1024
N_t, N_r	Number of transmit and receive antennas	512, 16
K_x, K_z	Number of subarrays at x- and z- axis of the BS	4, 2
L_t, L_r	Number of transmit and receive RF chains	8, 4
d_s	Subarray spacing	128λ
T_0	Frame interval	1 ms
q_a	Acceleration-noise strength in (36)	4, 9, 16
L_w	Length of sliding window	64

$D_R = \frac{2(S_b + S_u)^2}{\lambda} \approx 331$ m. UE positions are sampled in 3D coordinates within the NF with $D_1^1(\mathbf{p}) \sim \mathcal{U}[35 \text{ m}, 120 \text{ m}]$. For each position, we include a dominant LoS path determined by NF geometry and two additional NLoS paths. The corresponding channel realization is generated based on QuaDRiGa [31], adjusted by measurement-based statistics in urban microcell (UMi) environments obtained by our group [32], including K-factor, delay and angular spreads. In addition, the path powers are further scaled by frequency-dependent free-space loss and gaseous attenuation following ITU-R P.676. Comb-type FDM pilots are synthesized using the element-wise SWM, whereas the physics modules in Sec. II adopt the tractable HSPM to avoid inverse crime. For tracking, trajectories are generated by the state evolution in Sec. IV-A with frame interval T_0 and three mobility regimes with $q_a \in \{4, 9, 16\}$, where each is initialized with a random direction and speed $v \sim \mathcal{U}[10, 30]$ m/s. The above implementations ensure that the datasets preserve key NF parallax and THz propagation characteristics.

We generate $N_1 = 240,000$ static samples and $N_2 = 60,000$ trajectories, and divide them into train/validation/test sets (80%/10%/10%) at the sample level for the static dataset and at the trajectory level for the tracking dataset. Models are implemented in PyTorch and trained by AdamW with weight decay 10^{-2} and gradient clipping at 1.0. PAST is trained with batch size 256 for 200 epochs using a peak learning rate 2×10^{-4} with a 5-epoch linear warm-up followed by cosine decay to 10^{-6} , and then it is frozen to generate $\mathcal{E}(q)$ for TT. TT is trained with batch size 64 trajectories for 150 epochs using a peak learning rate 1×10^{-4} with the same schedule, and the ground truth is not injected into its inputs. λ_{phy}^t is linearly annealed from 0 to 0.2 over the first 30 epochs. Results are averaged over $R = 10$ random seeds. Experiments are conducted on a workstation equipped with $8 \times$ NVIDIA GeForce RTX 4090 GPUs (CUDA 12.4; Driver 550.90.07).

B. Performance of PAST

In this subsection, we evaluate the NF localization performance of PAST. For the static task, the UE state reduces to $\mathbf{x} = [\mathbf{p}^T, \mathbf{0}^T]^T$ and PAST outputs $\hat{\mathbf{p}}$. Moreover, we also compare it with four representative baselines, including (i) *JARE* [19]: a joint angle and range estimation method based on the DFT codebook, adapted by aggregating subarray-resolved pilot powers over the comb tones; (ii) *2D-MUSIC* [33]: a

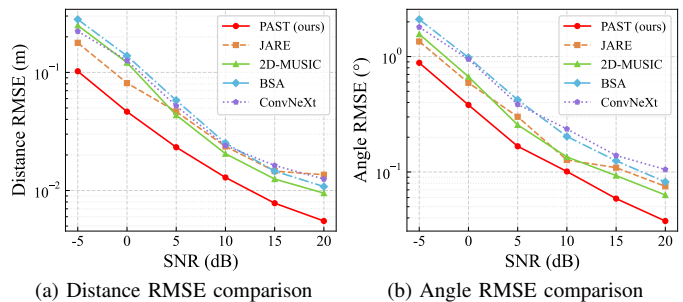


Fig. 3. Static RMSE comparison of different methods with SNR.

parametric estimator that performs a 2D spectral search on the NF manifold, with the sample covariance formed by wideband pilot snapshots; (iii) *BSA* [34]: a block-sparse-aware approach on a distance-dependent orthogonal dictionary, where the dominant component is recovered and mapped to the UE location through NF geometry; (iv) *ConvNeXt regression* [35]: a DL backbone baseline inspired by [35], and it is trained to regress the distance and angles from the same FDM pilot tensor of magnitude and phase-increment features, without reproducing the CBS or TTD front-end. All methods use the same array configuration, comb-type FDM pilots and FF DFT probing budget, and differ in the inference procedure. The accuracy is characterized by the distance and angle RMSEs averaged over subarrays, given by

$$\text{RMSE}(D) = \sqrt{\frac{1}{N_1 R K} \sum_{n=1}^{N_1} \sum_{r=1}^R \sum_{k=1}^K (\Delta D_{n,r}^k)^2}, \quad (60a)$$

$$\text{RMSE}(\angle) = \frac{180}{\pi} \sqrt{\frac{1}{N_1 R K} \sum_{n=1}^{N_1} \sum_{r=1}^R \sum_{k=1}^K (\Delta \angle_{n,r}^k)^2}, \quad (60b)$$

where $\Delta D_{n,r}^k = D_k(\hat{\mathbf{p}}_{n,r}) - D_k(\mathbf{p}_n)$ and $\Delta \angle_{n,r}^k = \arccos(\mathbf{u}_k^T(\mathbf{p}_n) \mathbf{u}_k(\hat{\mathbf{p}}_{n,r}))$.

As shown in Fig. 3, the accuracy of all methods improves with increased SNR, while PAST consistently achieves the lowest distance and angle RMSE across the tested SNR range. At -5 dB, PAST attains 0.102 m distance RMSE and 0.883° angle RMSE, and meanwhile, the strongest baseline is JARE with RMSE of 0.178 m and 1.35° . At 15 dB, the RMSE further improves to 7.81 mm and 0.0588° , and at 20 dB it reaches 5.52 mm and 0.0376° . For the high SNR regime, the best baseline is 2D-MUSIC, while PAST maintains clear gaps of 4.69 mm and 0.0342° at 15 dB. Among the baselines, JARE is the strongest at low SNR because it estimates angle from angular support and distance from DFT probing power ratios, which is less sensitive to phase statistics, but its improvement is limited at high SNR due to a finite probing resolution. 2D-MUSIC improves rapidly with SNR since more reliable sample covariance estimation yields cleaner subspace separation under the same pilot budget. BSA shows a similar SNR trend, but it can be affected by mismatch in the distance-dependent dictionary and the resulting leakage in block-sparse recovery. ConvNeXt regression also improves steadily with SNR and reaches 0.0125 m and 0.105° at 20 dB, but it remains inferior to the physics-structured PAST under the same pilot budget.

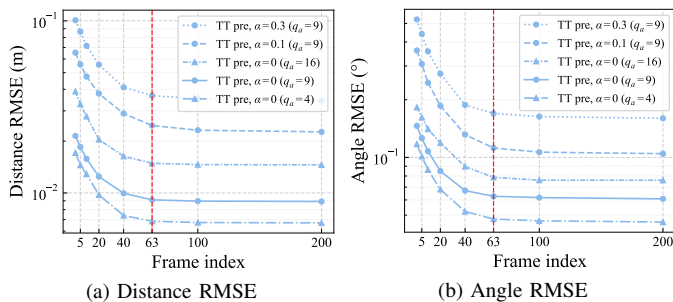


Fig. 4. Time evolution of TT prediction RMSE at SNR = 15 dB.

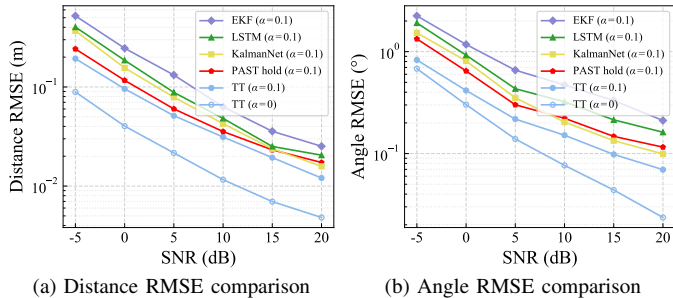


Fig. 5. Filtering RMSE comparison of different methods versus SNR with $\alpha = 0.1$ (TT with $\alpha = 0$ is shown as a reference).

C. Performance of TT

This subsection evaluates TT for online filtering and prediction in beam tracking, focusing on robustness to bad frames and the resulting closed loop beam benefit. Bad frames occur with rate α and are generated by applying an additional 20 dB attenuation to the pilot observation in the corrupted frames. We compare TT with four representative trackers, including (i) *PAST+hold*, which uses the current PAST output for both filtering and prediction, (ii) *EKF*, which applies an Extended Kalman Filter model with the PAST output as measurement [23], (iii) *LSTM*, which performs causal recurrent temporal modeling for proactive tracking [27] under the same measurement interface, and (iv) *KalmanNet*, which learns Kalman style updates under partially known dynamics [28] with the same state prior. All compared methods are causal, sharing the same frozen PAST front end with the same pilot budget.

Fig. 4 shows that at SNR = 15 dB, TT prediction RMSE converges within a window and stays stable under bad frames and different mobilities. At $q = 200$ with $q_a = 9$, the distance RMSE is 8.92 mm for $\alpha = 0$, increases to 0.0227 m for $\alpha = 0.1$, and reaches 0.0345 m for $\alpha = 0.3$. The corresponding angle RMSE follows the same trend and converges to 0.0608°, 0.105° and 0.160°, respectively. With $\alpha = 0$, increasing mobility from $q_a = 4$ to $q_a = 16$ raises the steady distance RMSE from 6.70 mm to 0.0146 m and the steady angle RMSE from 0.0461° to 0.0758°.

Fig. 5 compares filtering accuracy versus SNR, where TT performs the best with its strong robustness to bad frames. When $\alpha = 0.1$ and SNR = -5 dB, TT attains RMSE of 0.193 m and 0.829°, while the strongest baseline PAST+hold shows 25.4% higher distance RMSE and 60.9% higher angle RMSE. EKF is the weakest with RMSE of 0.521 m and

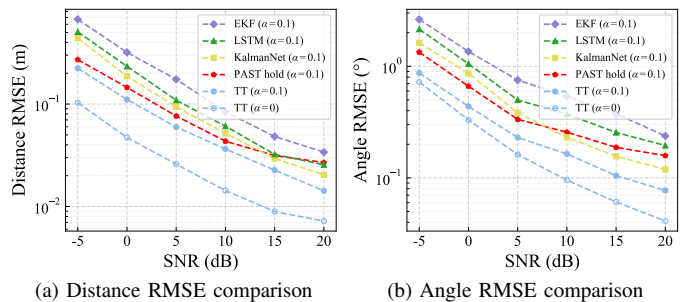


Fig. 6. Prediction RMSE comparison of different methods versus SNR with $\alpha = 0.1$ (TT with $\alpha = 0$ is shown as a reference).

2.25°. This ordering is consistent with how bad frames affect temporal inference. PAST+hold avoids error propagation but fails to exploit temporal smoothing, while EKF is more affected once an unreliable update occurs. KalmanNet improves upon EKF but still follows a recursive update flow [28]. At SNR = 20 dB, TT attains 0.0121 m and 0.0695°, with the best baseline KalmanNet exhibiting 31.2% and 42.7% higher distance and angle RMSE. The reference TT curve with $\alpha = 0$ reaches 4.82 mm and 0.0236° at SNR = 20 dB, indicating the ceiling imposed by the bad frame process.

Fig. 6 reports prediction accuracy, which determines the beam initialization for the next frame. At SNR = -5 dB, TT attains 0.223 m and 0.872°, compared with 0.271 m and 1.34° for PAST+hold, while EKF yields the largest RMSE of 0.670 m and 2.63°. At SNR = 20 dB, TT attains 0.0142 m and 0.0772°, while KalmanNet attains 0.0203 m and 0.118° as the best baseline. Prediction is more sensitive to occasional unreliable evidence and motion changes, where TT maintains the best prediction accuracy by aggregating the causal window and downweighting unreliable evidence through its reliability-injected attention, whereas LSTM is more likely to be affected by bad frame perturbations in the input without such explicit reliability handling [27].

The communication performance is evaluated by the single-stream spectral efficiency (SE), defined as

$$SE(q+1) = \frac{1}{M} \sum_{m=1}^M \log_2 \left(1 + \frac{\rho |\mathbf{w}_{eq}^H[m] \mathbf{H}[m] \mathbf{f}_{eq}[m]|^2}{\sigma_n^2} \right). \quad (61)$$

At the q^{th} frame, based on the prediction $\hat{\mathbf{p}}^{\text{pre}}(q+1)$, an effective unit-norm transmit beam $\mathbf{f}_{eq}[m]$ is constructed using the HSPM in Sec. II, with intra-subarray steering from the predicted local angles and inter-subarray phase from the predicted distances, while $\mathbf{w}_{eq}[m]$ is set as an ideal matched unit-norm combiner. The ideal NF alignment curve uses the true $\mathbf{p}(q+1)$, and the FF beams discard the distance and use only the global angle. As shown in Fig. 7, under a fixed transmit-power budget, corresponding to -0.1 dBm per subcarrier, our proposed method TT stays close to the optimal SE across the tested distances, and consistently outperforms FF steering and other tracking approaches even when bad frames occur. The SE of TT with $\alpha = 0$ is only 0.31 bps/Hz and 0.37 bps/Hz below the optimal SE at 35 m and 120 m, respectively. Ignoring the distance incurs up to 4.15 bps/Hz SE loss at

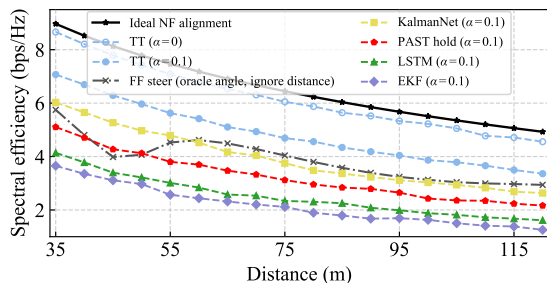


Fig. 7. Spectral efficiency comparison of different methods.

TABLE II
ABLATION STUDIES OF PAST ($\alpha = 0.1$, SNR = 15 dB)

Method	Distance RMSE (m)	Angle RMSE ($^\circ$)
PAST (full)	0.0232	0.147
w/o $c_{k,g}$ ($c_{k,g} = 1$)	0.0351 (+51.29%)	0.239 (+62.59%)
w/o $e_b, b_{ij}^{(h)}$	0.0263 (+13.36%)	0.195 (+32.65%)
w/o factorized fusion	0.0276 (+18.97%)	0.178 (+21.09%)
w/o $\mathcal{L}_{\text{phy}}^s$	0.0329 (+41.81%)	0.203 (+38.10%)

45 m which generally decreases with distance. It quantifies the importance of considering distance in NF communication.

D. Ablation Study

Ablation studies are conducted for PAST and TT. For module-level attribution, all TT variants are trained on the same evidence sequences $\{\mathcal{E}(q)\}$ from the frozen full PAST.

In Table II, we verify the necessity of key PAST components. First, removing the reliability gate by setting $c_{k,g} = 1$ causes the largest degradation, increasing the distance and angle RMSE by 51.29% and 62.59%. It highlights the role of reliability-aware evidence competition and aggregation in (25) and (27) and pooling in (28) under bad frames. Second, without the physics-in-the-loop regularizer $\mathcal{L}_{\text{phy}}^s$, the RMSE increases by 41.81% and 38.10%, demonstrating that the consistency constraint in (33) provides a strong physical anchor beyond supervised regression. Third, disabling the geometry priors e_b and $b_{ij}^{(h)}$ increases the angle RMSE by 32.65%, validating the geo-arm bias is essential for extracting parallax information. Excluding the factorized fusion with a single encoder also worsens performance, suggesting that the intra- and inter-subarray factorization aligns better with the array structure while being computationally efficient.

In Table III, the filtering and prediction RMSEs are reported at the first and the second line of each cell, respectively. Without reliability-injected attention $\mathcal{Q}(q)$, the filtering and prediction angle RMSEs increase by 45.77% and 60.95%, while removing the temporal physics loop $\mathcal{L}_{\text{phy}}^t$ also yields obvious degradation. These verify that strong robustness requires both reliability-aware aggregation in (50)-(51) and drift-consistent regularization in (58). In addition, dropping the increment descriptor $\mathbf{d}_k(q)$ mainly affects prediction, consistent with its role of injecting inter-frame delay and offset cues from (38) to (40) for forecasting. Removing the causal constraint in $\mathbf{M}(q)$ results in smaller yet consistent decline, supporting that strictly causal message passing with intra-frame bidirectional attention

TABLE III
ABLATION STUDIES OF TT ($\alpha = 0.1$, $q_a = 9$, SNR = 15 dB)

Method	Distance RMSE (m) (Filtering / Prediction)	Angle RMSE ($^\circ$) (Filtering / Prediction)
TT (full)	0.0194 0.0227	0.0981 0.105
w/o $\mathcal{Q}(q)$	0.0230 (+18.56%) 0.0293 (+29.07%)	0.143 (+45.77%) 0.169 (+60.95%)
w/o $\mathbf{d}_k(q)$ ($a_k = 0$)	0.0226 (+16.49%) 0.0289 (+27.31%)	0.108 (+10.09%) 0.155 (+47.62%)
w/o $\mathcal{L}_{\text{phy}}^t$	0.0228 (+17.53%) 0.0302 (+33.04%)	0.151 (+53.92%) 0.172 (+63.81%)
w/o causal $\mathbf{M}(q)$	0.0210 (+8.25%) 0.0253 (+11.45%)	0.112 (+14.17%) 0.129 (+22.86%)
w/o f_{fil}	0.0275 (+21.15%)	0.163 (+55.24%)

TABLE IV
COMPUTATIONAL COMPLEXITY COMPARISON

Method	Complexity
PAST (ours)	$\mathcal{O}(C_{\text{PAST}})$
JARE	$\mathcal{O}(PN_g)$
2D-MUSIC	$\mathcal{O}(K^2M + K^3 + N_gK^2)$
BSA	$\mathcal{O}(IPN_d)$
ConvNeXt regression	$\mathcal{O}(C_{\text{cnn}})$
PAST+EKF	$\mathcal{O}(C_{\text{PAST}} + n_a^3 + n_b^2n_b)$
PAST+LSTM	$\mathcal{O}(C_{\text{PAST}} + n_b d_r + d_r^2)$
PAST+KalmanNet	$\mathcal{O}(C_{\text{PAST}} + n_b d_k + d_k^2)$
PAST+TT (ours)	$\mathcal{O}(C_{\text{PAST}} + M + L_T(N^2d_T + Nd_Td_f))$

improves online generalization. Disabling the filtering head f_{fil} degrades prediction to 0.0275 m and 0.163 $^\circ$, highlighting the necessity of the dual-head design and the filtered-state anchor in (53) and (54b) for stable prediction.

E. Computational Complexity

Table IV compares the computational complexity of different methods under the same comb-type FDM pilot budget. For PAST, d_P is the latent width, L_a and L_b denote the numbers of layers in $\text{Enc}_{\text{intra}}(\cdot)$ and $\text{Enc}_{\text{inter}}(\cdot)$. Accordingly, the dominant per-frame PAST cost is $C_{\text{PAST}} = \mathcal{O}(M + L_a K G^2 d_P + L_b K^2 d_P)$. We report attention-dominated asymptotic complexity, where linear projections, FFN terms, causal masking and reliability injection only affect constant factors. For the baselines, P is the pilot-feature dimension, N_g is the polar-grid size, N_d is the dictionary size, I is the iteration number, n_a and n_b are the EKF state and measurement dimensions, d_r and d_k are the hidden widths of LSTM and KalmanNet, and C_{cnn} is the MAC count of ConvNeXt at the chosen input resolution.

Specifically, we use $d_T = 128$, $L_T = 4$ and $N_h = 8$. Measured on an RTX 4090, the runtime of PAST, TT frame-level tokenization and TT are $t_{\text{PAST}} = 0.29$ ms, $t_{\text{tok}} = 0.12$ ms and $t_{\text{TT}} = 0.32$ ms, respectively. Scheduling PAST and frame-level tokenization in parallel, the critical-path latency is $t_{\text{fr}} = \max\{t_{\text{PAST}}, t_{\text{tok}}\} + t_{\text{TT}} = 0.61$ ms. A conservative sequential upper bound is $t_{\text{seq}} = t_{\text{PAST}} + t_{\text{tok}} + t_{\text{TT}} = 0.73$ ms. Both are below the frame interval $T_0 = 1$ ms in Table I, leaving sufficient margin for beam update and data transmission.

VI. CONCLUSION

In this paper, we showed that the parallax effect can bridge low-overhead FF DFT codebook probing to accurate NF beam tracking in THz UM-MIMO without NF codebook sweeping. Comb-type FDM pilots create subarray-dependent frequency-affine phase signatures whose adjacent-tone and inter-frame increments provide delay and drift evidence while mitigating frame-wise common phase offsets. Guided by this physics-informed structure, PAST produces compact tokens with explicit reliability and delivers per-frame localization with a physics-in-the-loop consistency regularizer. TT then performs reliability-injected causal attention over a sliding window to jointly filter and predict the next-frame state for beam initialization, and it is further anchored by a temporal physics loop. Simulations confirm that at SNR 15 dB, PAST achieves 7.81 mm distance RMSE and 0.0588° angle RMSE, and with bad-frame rate $\alpha = 0.1$, TT achieves 0.0227 m distance and 0.105° angle prediction RMSE with 0.61 ms critical-path latency below frame duration. Future work will address stronger NLoS and blockage, measured datasets, hardware impairments, and multi-user settings.

REFERENCES

- [1] Z. Zeng and C. Han, "Parallax-aware spatial transformer: Fusing physics and learning for terahertz near-field localization," in *Proc. IEEE Int. Conf. Acoust., Speech, Signal Process. (ICASSP)*, May 2026.
- [2] A. Shafie, N. Yang, C. Han, J. M. Jornet, M. Juntti, and T. Kürner, "Terahertz communications for 6g and beyond wireless networks: Challenges, key advancements, and opportunities," *IEEE Netw.*, vol. 37, no. 3, pp. 162–169, May 2023.
- [3] I. F. Akyildiz, C. Han, and S. Nie, "Combating the distance problem in the millimeter wave and terahertz frequency bands," *IEEE Commun. Mag.*, vol. 56, no. 6, pp. 102–108, Jun. 2018.
- [4] C. Han, J. M. Jornet, and I. Akyildiz, "Ultra-massive mimo channel modeling for graphene-enabled terahertz-band communications," in *Proc. IEEE 87th Veh. Technol. Conf. (VTC Spring)*, Jun. 2018, pp. 1–5.
- [5] L. Yan, C. Han, and J. Yuan, "A dynamic array-of-subarrays architecture and hybrid precoding algorithms for terahertz wireless communications," *IEEE J. Sel. Areas Commun.*, vol. 38, no. 9, pp. 2041–2056, Sep. 2020.
- [6] L. Yan, Y. Chen, C. Han, and J. Yuan, "Joint inter-path and intra-path multiplexing for terahertz widely-spaced multi-subarray hybrid beamforming systems," *IEEE Trans. Commun.*, vol. 70, no. 2, pp. 1391–1406, Feb. 2022.
- [7] Y. Chen, L. Yan, C. Han, and M. Tao, "Millidegree-level direction-of-arrival estimation and tracking for terahertz ultra-massive mimo systems," *IEEE Trans. Wireless Commun.*, vol. 21, no. 2, pp. 869–883, Feb. 2022.
- [8] Y. Chen, C. Han, and E. Björnson, "Can far-field beam training be deployed for cross-field beam alignment in terahertz um-mimo communications?" *IEEE Trans. Wireless Commun.*, vol. 23, no. 10, pp. 14972–14987, Oct. 2024.
- [9] Y. Chen, H. Shen, and C. Han, "Cross far- and near-field beam management technologies in millimeter-wave and terahertz mimo systems," *IEEE Open J. Veh. Technol.*, vol. 7, pp. 73–107, Nov. 2025.
- [10] M. Cui and L. Dai, "Channel estimation for extremely large-scale mimo: Far-field or near-field?" *IEEE Trans. Commun.*, vol. 70, no. 4, pp. 2663–2677, Apr. 2022.
- [11] Y. Lu, Z. Zhang, and L. Dai, "Hierarchical beam training for extremely large-scale mimo: From far-field to near-field," *IEEE Trans. Commun.*, vol. 72, no. 4, pp. 2247–2259, Apr. 2024.
- [12] K. Chen, C. Qi, C.-X. Wang, and G. Y. Li, "Beam training and tracking for extremely large-scale mimo communications," *IEEE Trans. Wireless Commun.*, vol. 23, no. 5, pp. 5048–5062, May 2024.
- [13] M. Cui, Z. Wu, Y. Lu, X. Wei, and L. Dai, "Near-field mimo communications for 6g: Fundamentals, challenges, potentials, and future directions," *IEEE Commun. Mag.*, vol. 61, no. 1, pp. 40–46, Jan. 2023.
- [14] K. Chen, C. Qi, O. A. Dobre, and G. Ye Li, "Triple-refined hybrid-field beam training for mmwave extremely large-scale mimo," *IEEE Trans. Wireless Commun.*, vol. 23, no. 8, pp. 8556–8570, Aug. 2024.
- [15] C. You, Y. Zhang, C. Wu, Y. Zeng, B. Zheng, L. Chen, L. Dai, and A. L. Swindlehurst, "Near-field beam management for extremely large-scale array communications," *arXiv preprint arXiv:2306.16206*, Jun. 2023.
- [16] X. Shi, J. Wang, Z. Sun, and J. Song, "Spatial-chirp codebook-based hierarchical beam training for extremely large-scale massive mimo," *IEEE Trans. Wireless Commun.*, vol. 23, no. 4, pp. 2824–2838, Apr. 2024.
- [17] Y. Zhang, X. Wu, and C. You, "Fast near-field beam training for extremely large-scale array," *IEEE Wireless Commun. Lett.*, vol. 11, no. 12, pp. 2625–2629, Dec. 2022.
- [18] M. Giordani, M. Polese, A. Roy, D. Castor, and M. Zorzi, "A tutorial on beam management for 3gpp nr at mmwave frequencies," *IEEE Commun. Surveys Tuts.*, vol. 21, no. 1, pp. 173–196, Sep. 2018.
- [19] X. Wu, C. You, J. Li, and Y. Zhang, "Near-field beam training: Joint angle and range estimation with dft codebook," *IEEE Trans. Wireless Commun.*, vol. 23, no. 9, pp. 11890–11903, Sep. 2024.
- [20] S. Yang, X. Chen, Y. Xiu, W. Lyu, Z. Zhang, and C. Yuen, "Performance bounds for near-field localization with widely-spaced multi-subarray mmwave/thz mimo," *IEEE Trans. Wireless Commun.*, vol. 23, no. 9, pp. 10757–10772, Sep. 2024.
- [21] G. E. Garcia, G. Seco-Granados, E. Karipidis, and H. Wymeersch, "Transmitter beam selection in millimeter-wave mimo with in-band position-aiding," *IEEE Trans. Wireless Commun.*, vol. 17, no. 9, pp. 6082–6092, Sep. 2018.
- [22] W. Yi, W. Zhiqing, and F. Zhiyong, "Beam training and tracking in mmwave communication: A survey," *China Commun.*, vol. 21, no. 6, pp. 1–22, Jun. 2024.
- [23] S. Shaham, M. Kokshoorn, M. Ding, Z. Lin, and M. Shirvanimoghadam, "Extended kalman filter beam tracking for millimeter wave vehicular communications," in *Proc. IEEE Int. Conf. Commun. Workshops (ICC Workshops)*, Jul. 2020, pp. 1–6.
- [24] S. G. Larew and D. J. Love, "Adaptive beam tracking with the unscented kalman filter for millimeter wave communication," *IEEE Signal Process. Lett.*, vol. 26, no. 11, pp. 1658–1662, Nov. 2019.
- [25] C. Zhang, D. Guo, and P. Fan, "Tracking angles of departure and arrival in a mobile millimeter wave channel," in *Proc. IEEE Int. Conf. Commun. (ICC)*, Jul. 2016, pp. 1–6.
- [26] H. Wang, H. Li, J. Fang, and H. Wang, "Robust gaussian kalman filter with outlier detection," *IEEE Signal Process. Lett.*, vol. 25, no. 8, pp. 1236–1240, Aug. 2018.
- [27] S. H. Lim, S. Kim, B. Shim, and J. W. Choi, "Deep learning-based beam tracking for millimeter-wave communications under mobility," *IEEE Trans. Commun.*, vol. 69, no. 11, pp. 7458–7469, Nov. 2021.
- [28] G. Revach, N. Shlezinger, X. Ni, A. L. Escoriza, R. J. G. van Sloun, and Y. C. Eldar, "Kalmannet: Neural network aided kalman filtering for partially known dynamics," *IEEE Trans. Signal Process.*, vol. 70, pp. 1532–1547, Mar. 2022.
- [29] Y. Wang, C. Qi, W. He, and A. Nallanathan, "Near-field beam training and tracking with deep learning for extremely large-scale mimo," *IEEE Trans. Veh. Technol.*, vol. 74, no. 12, pp. 19783–19788, Dec. 2025.
- [30] S. K. Dehkordi, M. Kobayashi, and G. Caire, "Adaptive beam tracking based on recurrent neural networks for mmwave channels," in *Proc. IEEE 22nd Int. Workshop Signal Process. Adv. Wireless Commun. (SPAWC)*, Nov. 2021, pp. 1–5.
- [31] S. Jaeckel, L. Raschkowski, K. Börner, and L. Thiele, "Quadriga: A 3-d multi-cell channel model with time evolution for enabling virtual field trials," *IEEE Trans. Antennas Propag.*, vol. 62, no. 6, pp. 3242–3256, Jun. 2014.
- [32] Y. Li, Y. Wang, Y. Lyu, Z. Yu, and C. Han, "220 ghz urban microcell channel measurement and characterization on a university campus," in *Proc. IEEE Globecom Workshops (GC Workshops)*, Dec. 2024, pp. 1–5.
- [33] D. Gürgünoğlu, A. Kosasih, P. Ramezani, Ö. T. Demir, E. Björnson, and G. Fodor, "Performance analysis of a 2d-music algorithm for parametric near-field channel estimation," *IEEE Wireless Commun. Lett.*, vol. 14, no. 5, pp. 1496–1500, May 2025.
- [34] H. Wang, J. Fang, H. Duan, and H. Li, "Near/far-field channel estimation for terahertz systems with elaas: A block-sparse-aware approach," *arXiv preprint arXiv:2404.05544*, Sep. 2024.
- [35] H. Lei, J. Zhang, H. Xiao, D. W. K. Ng, and B. Ai, "Deep learning-based near-field user localization with beam squint in wideband xl-mimo systems," *IEEE Trans. Wireless Commun.*, vol. 24, no. 2, pp. 1568–1583, Feb. 2025.